# Diagnostics of Lithium Ion Batteries

Master Thesis
Georgios Krikis

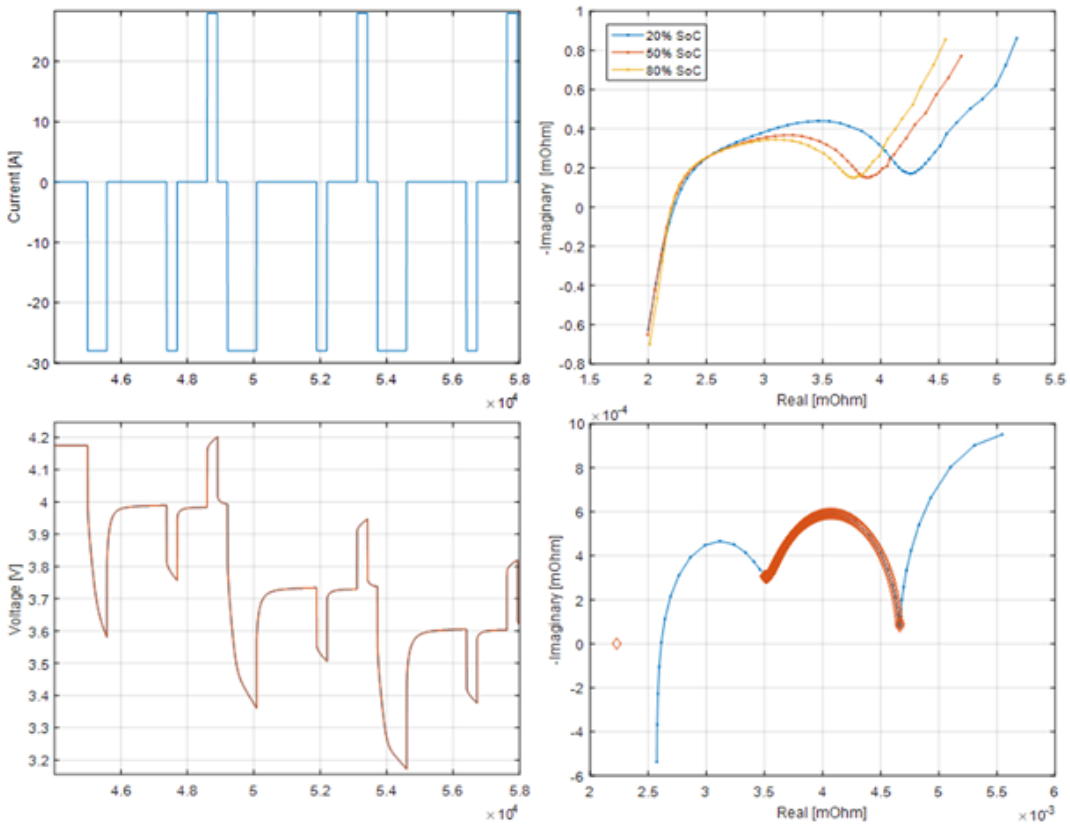


Energy Technology Department
Aalborg University, Denmark
January 5, 2018

AALBORG UNIVERSITY
STUDENT REPORT

Energy Technology Department
Pontoppidanstræde 111
9220 Aalborg Øst

**Title:**

Diagnostics of Lithium Ion Batteries

**Project:**

Master Thesis

**Project period:**

06-02-2017 to 05-01-2018

**Project group:**

PED946

**Participants:**

Georgios Krikis

**Supervisors:**

Erik Schaltz
Daniel-Ioan Stroe

Abstract:

This project intends to analyse the state-of-the-art methods that are used for diagnostics of Lithium ion batteries. First, a description of the performance parameters is presented with the dependencies that each need to encounter. Then, two state-of-the-art measurement techniques that can be used as diagnostic tools are presented and the special features that each method offers are presented along with the battery ageing. These methods are : (a) DC current pulses and (b) Electrochemical Impedance Spectroscopy (EIS). Both methods are implemented on a tested Lithium ion Nickel Manganese Cobalt (NMC) cell and the results are analysed in order to diagnose degrading performance parameters. An alternative method that employs Pseudo Random Binary Sequence (PRBS) signals is investigated through simulation software tools and is presented as an alternative method to apply diagnostic tests on Lithium ion batteries.

**Page count: 75 pages**
**Hand in date: 5. January 2018**

# Preface

The references are cited with the use of The American Institute of Physics (AIP) referencing method, which means that sources will be cited as "[n]", where n is the order of appearance. In the Bibliography chapter, they will be listed in the same manner. Illustrations will be labelled under the chapters they belong to and not the different sections they are included in. As an example, the first figure in Chapter 1 will be labelled "Figure 1.1", followed by 1.2, 1.3, etc. Tables and Equations follow the same principles.

As sincere as possible, I would like to thank my supervisors, Prof. Erik Schaltz and Assistant Professor Daniel Ioan Stroe for being next to me and providing all the needed help and support during the progress of this project from day one. This topic was a totally untouched area for me with not enough background knowledge, and even though, both my supervisors guided me all the way for my initial understanding even to the last moment. Working with them was a valuable experience for me.

It is very important for me to also thank PhD candidates Jacob Bitsch Norgaard and Theodoros Kalogiannis for sharing their knowledge in simulation tools, and for the useful discussions that helped to gain an intuitive understanding.

Last but not least, I would like to thank my family and my friends for their positive thoughts and support during the hard times and good times the whole period of this project.

Georgios Krikis

# Table of Contents

# List of Figures

# List of Tables

## 0.1 Nomenclature

| | |
|---|---|
| $Q$ | Capacity |
| $Q_{measured}$ | Measured Capacity |
| $Q_{BOL}$ | Measured Capacity at Beginning of Life |
| $R$ | Resistance |
| $R_{measured}$ | Measured Resistance |
| $R_{BOL}$ | Measured Resistance at Beginning of Life |
| $SOH_Q$ | State of Health in terms of Capacity |
| $SOH_R$ | State of Health in terms of Resistance |
| $SOH_{EV}$ | State of Health in terms of Electric Vehicles |
| $C$ | Capacity |
| $I$ | Current |
| $V$ | Voltage |
| $SOC_0$ | Initial State of Charge |
| $R_i$ | Internal Resistance |
| $R_{ohmic}$ | Ohmic Resistance |
| $R_{ct}$ | Charge Transfer Resistance |
| $R_{diff_pol}$ | Diffusion Polarization Resistance |
| $PPC_c$ | Charge Pulse Power Capability |
| $PPC_d$ | Discharge Pulse Power Capability |
| $V_{max}$ | maximum Voltage |
| $V_{min}$ | minimum Voltage |
| $C_{20s}$ | Capacitance associated with charge transfer resistance |
| $tau$ | time constant tau |
| $L$ | Inductance |
| $X_L$ | Inductive Reactance |
| $X_C$ | Capacitive Reactance |
| $Z$ | Impedance |
| $omega$ | Angular frequency |
| $Real_Z$ | Real part of complex impedance |
| $Imag_Z$ | Imaginary part of complex impedance |
| $f_{max}$ | maximum frequency |
| $f_{min}$ | minimum frequency |
| $f_c$ | Clock frequency |
| $T_{prbs}$ | Time period of PRBS |
| $L_s$ | Series Inductance of ac impedance parameters |
| $R_s$ | Ohmic Resistance of ac impedance parameters |
| $R_1$ | Resistance due to solid electrolyte interface of ac impedance parameters |
| $C_1$ | Capacitance associated with solid electrolyte resistance of ac impedance parameters |
| $R_2$ | Resistance due to charge transfer of ac impedance parameters |
| $C_2$ | Capacitance associated with charge transfer resistance of ac impedance parameters |
| $R_3$ | Resistance due to diffusion polarization of ac impedance parameters |
| $C_3$ | Capacitance associated with diffusion polarization of ac impedance parameters |
| $C_{fade}$ | Capacity fade |

## 0.2 Acronyms and Abbreviations

| | |
|---|---|
| EV | Electric Vehicle |
| ESS | Energy Storage Systems |
| PHEV | Plug-in Hybrid Electric Vehicle |
| UPS | Uninterrutable Power Supply |
| Li-ion | Lithium Ion |
| NiMH | Nickel metal Hybrid |
| BOL | Beginning of Life |
| EOL | End of Life |
| SOC | State of Charge |
| DOD | Depth of Discharge |
| SOH | State of Health |
| RUL | Remaining Useful Lifetime |
| EIS | Electrochemical Impedance Spectroscopy |
| Ah | Ampere per hour |
| ICE | Internal Combustion Engine |
| OCV | Open Circuit Voltage |
| LFP | Lithium Ion Phosphate |
| PPC | Pulse Power Capability |
| DC | Direct Current |
| AC | Alternating Current |
| EEC | Electrical Equivalent Circuit |
| PRBS | Pseudo Random Binary Sequence |
| LFSR | Linear Feedback Shift Register |
| FFT | Fast Fourier Transform |
| RPT | Reference Performance Test |
| NMC | Nikel Manganese Cobalt |
| CC-CV | Constant Current - Constant Voltage |
| NRMSE | Normalized Root Mean Square Error |

# 1 Introduction

Batteries are one of the most promising technologies nowadays as they are found in all portable electronic devices, in both electric vehicles (EV) and plugin hybrid electric vehicles (PHEV), but also in energy storage systems (ESS), and uninterruptable power supplies (UPS). One of the main reasons that motivate the research and development is the challenge of energy transition from fossil fuels to renewable and sustainable energy. Specifically, the Paris Agreement targets about reducing gas emissions that cause global warming [17], have provoked innovative changes in most of the energy consuming fields. The automotive industry and generally the utilization of electrical transportation in all means, is a key parameter to the goal of eliminating environmental pollution. Consequently, most of the developed countries in Europe, have made new policies and regulations to facilitate the concept of energy transition. For instance, in Norway gas combustion vehicles will be banned by the year of 2025, while in Germany and Great Britain the same policy will be applied by 2030 and 2040 [18]. This has led automotive manufacturers to align their future production lines accordingly where Tesla Motors was dominating so far, however, the Swedish Volvo automaker announced to include an electric motor in all models by 2019, meaning that their automotive production will be solely focused on EVs and PHEVs [19]. Both EVs and PHEVs, have a revolutionary construction compared to conventional automobiles. This is due to the powerful battery packs employed, that are either at the entire area capable of high performance demands and autonomy, or in a specific area of the vehicle that provides alternative switching to electrical power source along with the combustion engine as illustrated in Figure 1.1

Figure 1.1: (Left) Volvo XC90 plugin hybrid PHEV with battery pack located in the centre of the vehicle. (Right) Tesla model S full EV with battery pack located at entire area of the bottom vehicle [1]

## 1.1 Background information: Lithium-ion Battery Packs and Basic Characteristics

Batteries and the cells they contain are distinguished between primary and secondary. What makes them different is that the primary are not rechargeable, while the secondary cells have the advantage of being recharged. From secondary batteries, lithium-ion (Li-ion) cells, are gaining the most attention in the automotive industry because of the many advantages over other chemistries, such as the high operating voltage as shown in Figure 1.2 2 and the high energy density as shown in Figure 1.3.

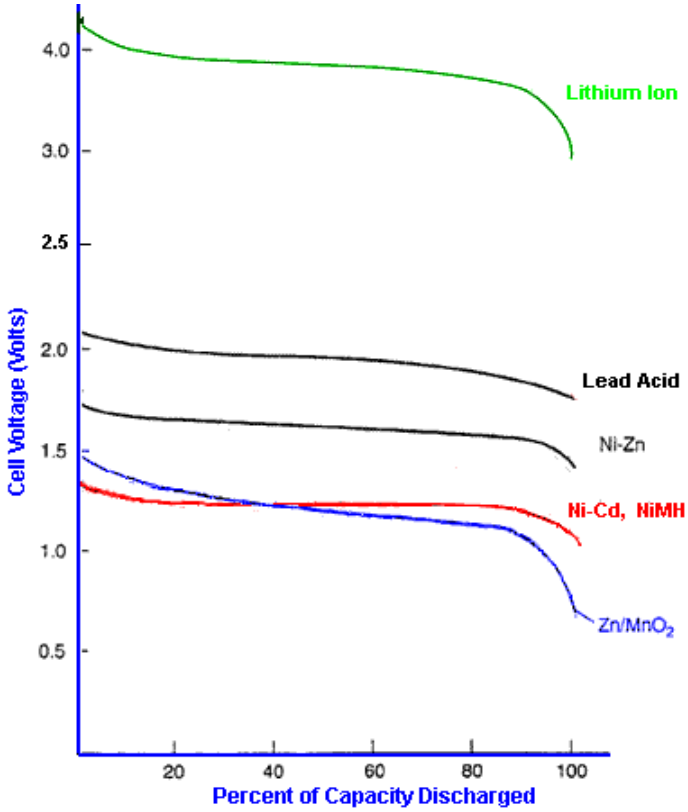


Figure 1.2: Secondary batteries voltage profile [2]

The energy density is distinguished between gravimetric and volumetric depending on the measurement that is taken with respect to the weight or size. Lithium ion batteries have high cell potential and along with the low weight of lithium metal, result in high energy and power output per unit of mass. Hence, the gravimetric energy of lithium ion batteries is remarkably higher in comparison to most secondary batteries for energy storage applications [20]. Finally, this simply means that the energy stored in the same physical battery size is much greater than other chemistries.

With several advantages over the most options, lithium ion batteries are nowadays preferred in most of the applications. They are available in diverse shapes and chemistries for which comparisons have been done in previous work [4] to specify the suitability in most applications as shown in Figure1.4

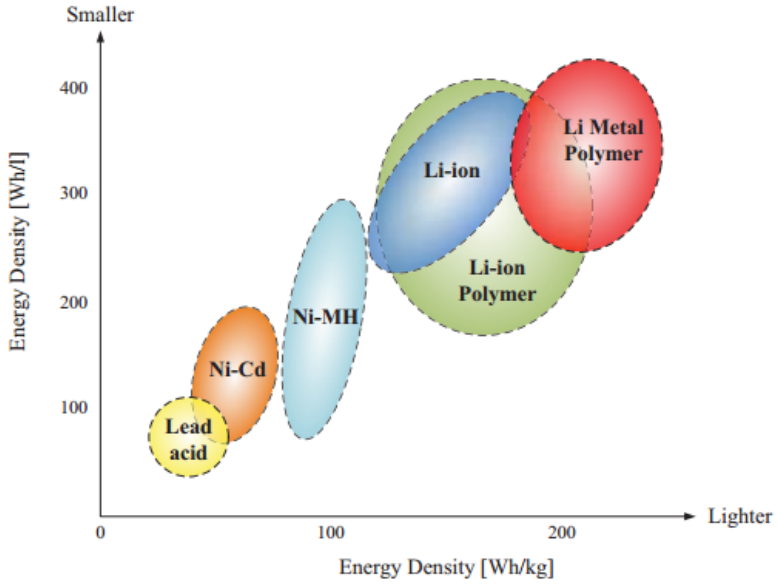


Figure 1.3: Comparison of batteries in both gravimetric and volumetric energy density [3]

| Applications | | Li-ion battery chemistries | | | | | | |
|---|---|---|---|---|---|---|---|---|
| | | LCO | LMO | LNO | NCA | NMC | LFP | LTO |
| Stationary | Grid frequency regulation | | | ✓ | | ✓ | ✓ | ✓ |
| | Forecast accuracy improvement | | | | ✓ | ✓ | ✓ | |
| | Power gradient reduction | ✓ | ✓ | ✓ | ✓ | ✓ | ✓ | ✓ |
| Automotive | EV | ✓ | ✓ | | ✓ | ✓ | ✓ | |
| | HEV | ✓ | ✓ | | ✓ | ✓ | ✓ | ✓ |
| | PHEV | | ✓ | | ✓ | ✓ | ✓ | |
| Back-up | UPS | | | ✓ | ✓ | ✓ | | |

Figure 1.4: Comparison of different Li-ion chemistries based on applications use[4]

Along with Lithium-ion, Lead acid, Sodium sulphur, and Nickel metal (NiMH) are some of the most popular chemistries among the several possible battery technologies that exist nowadays [21].

### 1.1.1 Ageing Definitions: Lifetime, Calendar Ageing and Cycle Ageing

The lifetime of a battery depends on several electrochemical and physical mechanisms that degrade with the usage and with the simple storage when no load is connected (open-circuit). The degradation, has a direct impact to the electrical performance and is caused in terms of increasing impedance, capacity fade and loss of power capability [22]. When these performance parameters reach a limit compared to the beginning of life (BOL) the battery can no longer be exploited, and this condition is referred to as the end of life (EOL). Calendar aging, is referred to the time when a battery is kept in idle state -no load connected, as in storage-. It is very

important here to have knowledge of two conditions when the battery is kept "on shelf". These are the state-of-charge (SOC) of the battery, and the temperature. In this case, the battery is not connected to any load, thus no operation is taking place and the only discharge possible might be by inevitable self-discharge. In cycle aging, the battery is assumed to be in operation mode, delivering or absorbing charge. Here, more parameter dependencies are present from the moment that a load or loads of current is applied. Additional to the calendar aging parameters, is the depth of discharge (DOD) but also the C-rate of the load current which is defined as the ratio between the load current (drawn or supplied) by the nominal capacity. Figure 1.5 shows how the number of cycles decrease with the increasing of DOD, while in TABLE 2 the considered parameters of each case are listed.

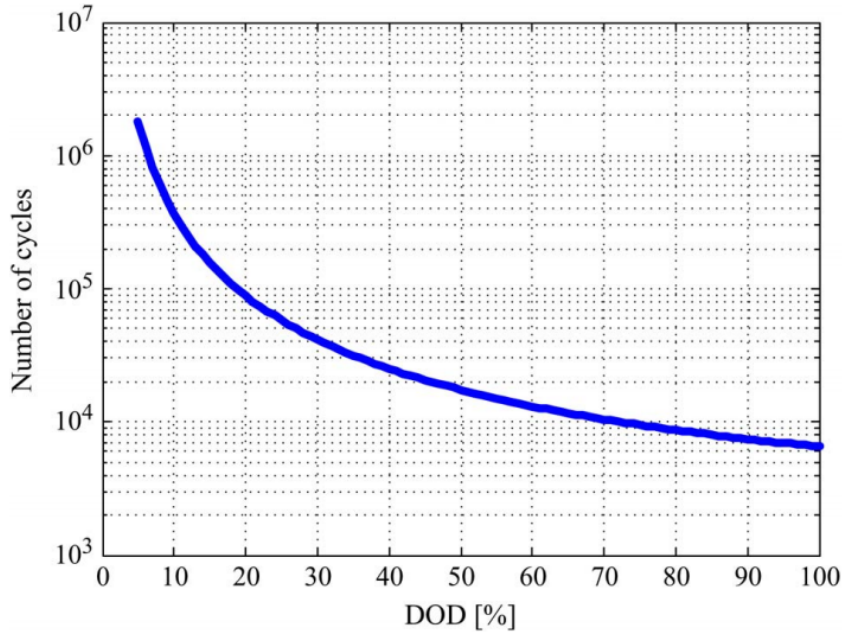


Figure 1.5: A Hypothetical battery lifetime curve that depicts the DOD effect vs number of cycles to EOL taken from [5]

| **Calendar life conditions** | **Cycle life conditions** |
|---|---|
| 1. State of Charge (SOC) | 1. State of Charge (SOC) |
| 2. Temperature | 2. Temperature |
| - | 3. Load Current |
| - | 4. Depth of Cycle |

Table 1.1: Parameters that are considered in each case of calendar and cycle life

## 1.2 Problem Statement

The vast improvements of electric mobility, require a solid infrastructure of charging stations and maintenance repairers with appropriate diagnostic tools that would meet the upcoming challenges. EVs, depend on the battery, in a manner that the entire operating system, from accelerating to braking and all the involved facilities rely on the battery capabilities. The electrochemical and physical degradation of batteries' interior and exterior, have a direct impact on the electrical performance in terms of increasing impedance, rising temperature, capacity fade and loss of power capability. This effect of degradation is finalized when a battery has reached the EOL. Thus, by monitoring the state-of-health (SOH), drivers of EVs and PHEVs would be able to predict the remaining useful lifetime (RUL). Although measurement techniques exist, these methods are limited to lab conditions and are not applicable without disassembling the battery pack from an EV or PHEV. Still there is no tool that would provide information about the SOH regarding the current battery performance during a typical maintenance inspection.

## 1.3 Main Objectives

The objective of this master thesis is to investigate the state-of-the-art methods that are used for battery diagnostics of impedance increase and present the special features that each method offers. The results obtained from each method will be demonstrated from an experimental point of view, and finally a new method based on pseudorandom binary sequence signals will be demonstrated in simulation manner in order to verify the simulation feasibility of being used as an alternative for EIS. In order to reach this aim, the following steps were taken:

- In-depth study of literature regarding definitions, state of art diagnostic methods and measurement techniques
- Investigation of state-of-the-art measurement principles and practically apply on tested cell in the battery lab of the university.
- Apply two investigated state-of-the-art measurement techniques on the raw data obtained from a tested cell , in order to measure the status of performance parameters.
- Derive an impedance model that would replicate the actual impedance behaviour obtained from the applied measurements with the least error.
- Analysis of the obtained parameters and their trends of evolution through calendar aging, at 20% 50% and 80% SOC.
- Achieve simulation feasibility of a modified method that would measure multiple targeted frequencies at once, applied on the previous derived impedance model
- Examine the results of the two applied methods and evaluate the simulation results of the simulated method
- Present the most affected SOC level, frequency range, and calendar condition in which the most degradation occurred.

## 1.4 Assumptions and Limitations

- This master thesis studies and experiments are done based on a single battery cell and not on a pack size level.
- The ageing effect is studied with regards to calendar ageing without considering cycle ageing.
- Due to time limitation, the demonstration of calendar ageing is performed in lab conditions and in accelerated manner. This is achieved by keeping the cell in constant high temperature of 40 °C through each monthly storage time
- This study is done from electrical point of view, focusing on the diagnosis of electrochemical parameters represented by electrical components.
- The modelling process is limited to an impedance model without investigating the modelling of other perspectives.
- Capacity and state of charge computations are limited to Coulomb and Ampere hour counting methods. Other methods are mentioned but not investigated.
- A Lithium ion battery cell of the chemistry Nikel Manganese Cobalt/Graphite (NMC) is used as representation of secondary (rechargeable) battery. Other chemistries are not part of the project scope as the aim is to validate a diagnostic tool and not to find the most suitable Li-ion chemistry.

## 1.5 Project Outline

This project is divided in 7 chapters which are briefly described below:

In Chapter 2, The basic definitions of parameters related to the performance of batteries are introduced, by presenting the fundamental expressions and illustrations of the dependencies that influence the performance of each parameter.

In Chapter 3, The state-of-the-art methods that are commonly used in the literature regarding li-ion battery diagnostics are presented and the measurement techniques are introduced.At the last part of this chapter an introduction to the design of a random signal is presented that can be used as an excitation signal for purpose similar to the other presented techniques.

In Chapter 4, The implementation of diagnostic methods is performed on a tested cell, and the results are analysed in order to demonstrate the information that each technique can offer.

In Chapter 5, the simulation of pseudorandom binary sequence (PRBS) is shown on an impedance model in order to validate the feasibility of usage as an alternative diagnostic tool.

In Chapter 6,Conclusions of the results by the three methods are discussed.

In Chapter 7, the potential of future work based on the simulation results obtained by the pseudorandom binary sequence signals is discussed.

# Part I

# Theory

# 2 Battery States and Parameters

## 2.1 State of Health

The state of health (SOH), is the measurement of a battery's condition compared to the BOL. The battery's SOH is the current information regarding the degradation in terms of lifetime, capacity fade, increase of internal resistance or even in power capability. The following Figure 2.1, presents the corresponding meaning of SOH along with EV applications where the EOL is defined when the remaining capacity has reached the 80% of the BOL capacity [23], and where in terms of internal resistance, the $R_i$ has been doubled compared to BOL [5].

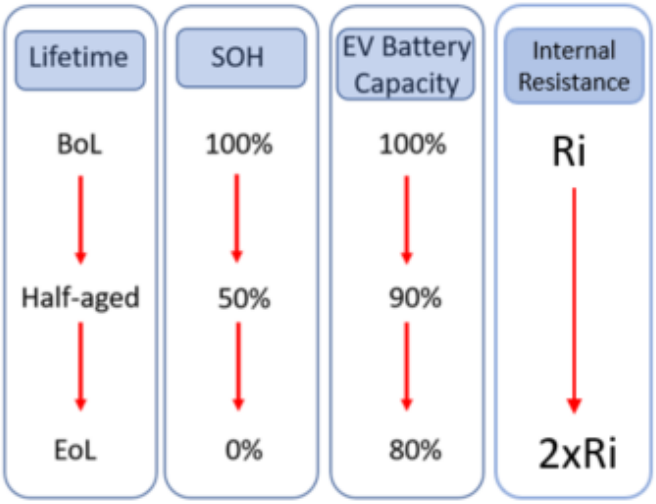


Figure 2.1: Parallel illustration of various terms that SOH is expressed through.

The SOH is expressed through equations from equation 2.1 to equation 2.2 however the SOH for EV applications is modified to equation 2.3 based on [24].

$$SOH_Q = \frac{Q_{measured}}{Q_{BOL}} \times 100 \tag{2.1}$$

$$Or: \qquad SOH_R = (2 - \frac{R_{measured}}{R_{BOL}}) \times 100 \tag{2.2}$$

$$And\ for\ EVs: \qquad SOH_{EV} = \left( \frac{\frac{Q_{measured}}{Q_{BOL}} - 0.8}{0.2} \right) \times 100 \tag{2.3}$$

## 2.2 Capacity

The battery capacity is defined as the maximum amount of charge that a battery can deliver or absorb, and is measured in Amperes per hour (Ah) or Watts per hour when mentioned as specific energy. Along with the lifetime of the battery and the operating conditions, the nominal capacity will be decreasing accordingly. A commonly used method and considered the simplest for estimating the capacity is the Coulomb counting [6], which is based on the integration of current that flows in and out of a battery during a full charge or discharge. However, many approaches and measurement techniques are found in the recent literature for estimating the battery's capacity and the dependencies on operating conditions [25]. Figure 2.2 and Figure 2.3 show the dependency of capacity on temperature and load current. The actual capacity is estimated through the following expression in equation 2.4.

$$C = Q(Ah) = \int I(t)dt \tag{2.4}$$

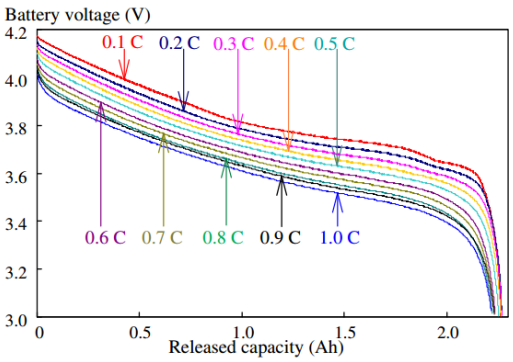


Figure 2.2: Battery voltage and capacity for various c-rates [6]

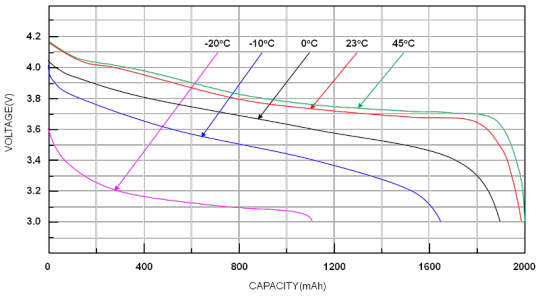


Figure 2.3: Capacity after temperature effect taken from [7]

## 2.3 State of Charge (SOC)

By having the knowledge of a battery's capacity, it is possible to define a fully charged state for the battery. Based on this value, the state of charge (SOC) is estimated as shown in equation 2.5 from which the result is basically the available or releasable capacity left. The SOC is very important for the automotive industry of EVs and HEVs since it is the analogy of a usual fuel gauge in conventional internal combustion engine (ICE) vehicles. For estimating the SOC, the Amp-hour counting method, is the most commonly used technique.This is because of certain advantages such as the low cost of measurement equipment, the low computational power needed, and the possibility to combine with other techniques [26]. According to this study, many possibilities involving models, observers, or other static characteristics of the battery exist in order to estimate the SOC. The Amp-hour counting method, however, is the most common as it simply employs the following equation:

$$SOC = SOC_0 - 100 \cdot \frac{\int_0^t I(t)dt}{C} \tag{2.5}$$

Where:

- $SOC_0$ is the initial state of charge of the battery [%]
- I is the current flowing through the battery, positive if discharging [A]
- C is the capacity of the battery [Ah]

## 2.4 Open Circuit Voltage(OCV)

The OCV is defined as the voltage across the electrodes of the battery in a no-load condition (i.e. when no current is flowing through the cell), and is an important parameter for the accurate estimation of a battery's power capability as presented later in this chapter. The OCV depends on the thickness of the electrolyte [27], the temperature [28], the operation history of the battery, the SoC [8], but also on whether the battery is charging or discharging as shown in Figure 2.4 (Right). In Figure 2.4 (Left) as presented in [9], the 100% SoC of a Lithium Iron Phosphate tested battery, corresponds to the upper voltage threshold 3.6V while the 0% to the lower voltage limit 2.0V. Based on this relationship as demonstrated in [26] the OCV can be used as input to SoC estimation techniques that are based on relaxation time after current interruption.

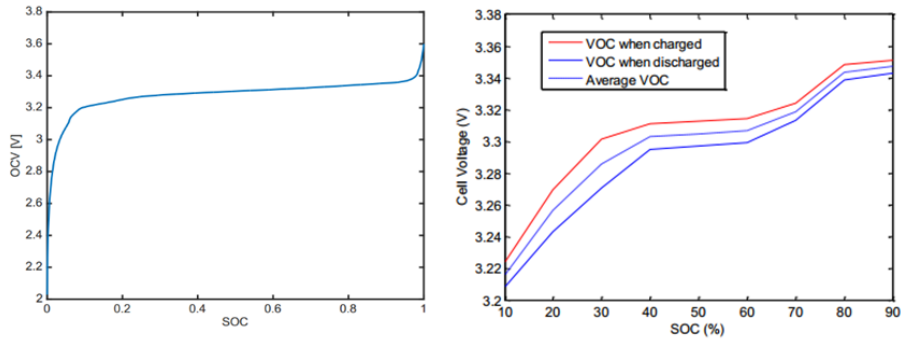


Figure 2.4: (Left) OCV-SoC curve of a LFP cell from 0% SOC(2.0V) to 100% SOC (3.6V) [8] (Right) OCV measured during charge and discharge for LFP [9]

## 2.5 Internal Resistance(IR)

The resistance of any electrical system is perhaps the parameter that determines mostly the flow of current, the power dissipation, and the same rule implies for electrochemical batteries regarding charging and discharging processes. Internal resistance though, is the actual definition of a battery's resistance and is the summary of different effects that take place in each cell. Specifically, these are electron conductivities, charge transfer effects, and diffusion polarization processes [29], which all together define internal resistance as expressed in equation 2.6

$$R_i = R_{ohmic} + R_{ct} + R_{diff\_pol} \tag{2.6}$$

The internal resistance shows many dependencies some of which rely on the SOC, the C-rate, the temperature and the SOH [30]. In Figure 2.5 from [10] and [11], the influences of different SoC levels and temperature variations applied on a LFP battery are shown.

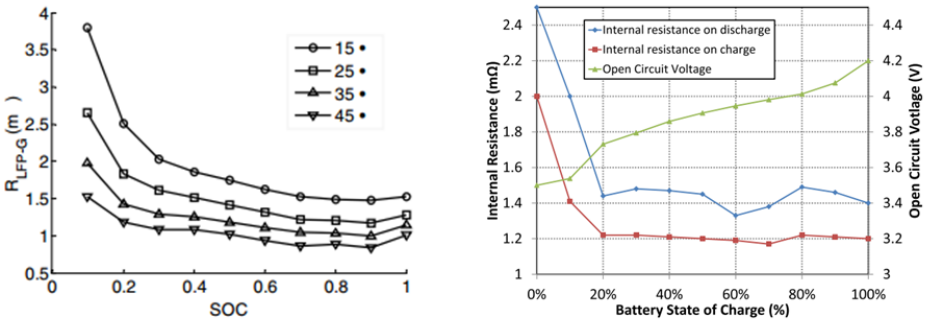


Figure 2.5: (Left) Internal resistance change with temperature for LFP battery [10] (Right) Charge and discharge internal resistance are different from each other along with OCV and SoC [11]

## 2.6 Pulse Power Capability(PPC)

The performance behaviour of any application that employs Li-ion batteries, depends on the pulse power capability of the battery that is used as its main power supply according to [31] and is expressed in 2.7 and 2.8. For example, in EV applications, the parameter that determines the acceleration, is the power capability of the battery which follows the same principle as capacity, since it decreases along with the battery's ageing but not proportionally due to different dependecies. Both in terms of calendar and cycle aging, the more internal resistance increases, the more power capability decreases. However, by having a closer look to the equations one can easily realize that when estimating power capability, the OCV is also involved according to [12]. This directly means that the pulse power capability will not decrease linearly with internal resistance decrease because the OCV involved follows an inverse trend. In Figure 2.5 (Right) from [11] this inverse relationship can be clearly noticed.

$$PPC_c = \frac{V_{max} - OCV}{R_i} \times V_{max} \tag{2.7}$$

$$PPC_d = \frac{OCV - V_{min}}{R_i} \times V_{min} \tag{2.8}$$

Where $R_i$ the internal resistance and $V_{min}$ and $V_{max}$ are the lowest and highest voltage responds at the end of each pulse as shown in Figure 2.6

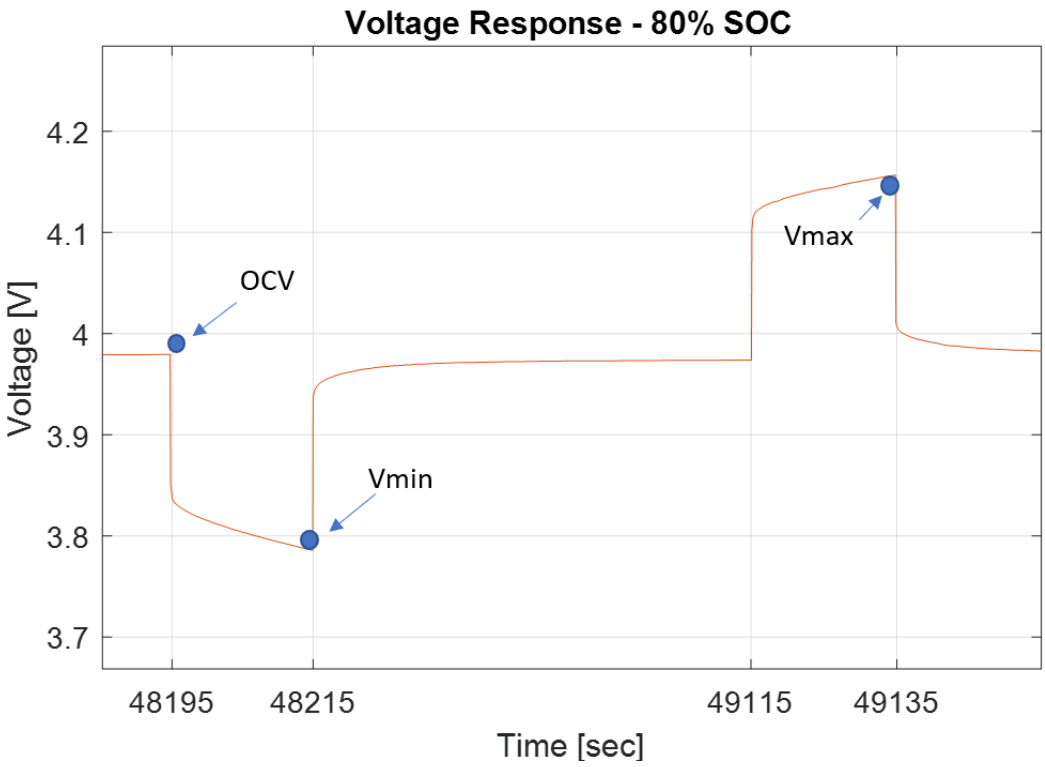


Figure 2.6: Illustration of the OCV measurement,and considered $V_{min}$ and $V_{max}$ during a discharge an charge pulse.

# 3 State of the Art Measurement Techniques for Internal Resistance and AC Impedance

## 3.1 DC Current Pulses

Dc current pulses are widely used for determining internal resistance also referred to as dc impedance or direct current resistance DCR in the literature. With repetitive current pulses at any SOC level, the internal resistance and the pulse power capability that Li-ion batteries exhibit are determined under various operating conditions. Different ways of exploiting this technique are described in [32]. Nevertheless, the most common method that is also employed in this master thesis, is the current injection method. Charge and discharge current pulses are applied on a tested cell and the internal resistance is determined by measuring the voltage response during the applied current pulse. By dividing the voltage response to instantaneous and transient regions the internal resistance can be determined from the differential voltage measurements. In Figure 3.1 an exemplification of this description is illustrated with battery current and voltage during a discharge current pulse.

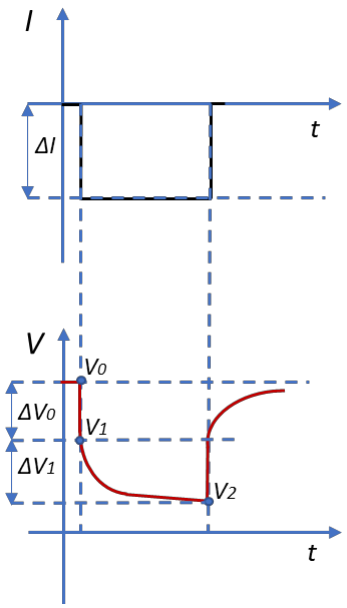


Figure 3.1: Representation of a discharge current pulse applied to a battery with the voltage drop response below

According to [30], in power applications a current pulse of just a few milliseconds would be enough to determine the corresponding ohmic resistance that limits the power capability. However, in EV applications, the current pulse should last between 10 - 20 seconds, as this is the time the delivered power would enable the desired acceleration demanded by the driver. The two resistances determined for each case are found through the following equations 3.1 and 3.2.

$$R_{ohmic} = \frac{\Delta V_0}{\Delta I} = \frac{\mid V_0 - V_1 \mid}{\mid I \mid} \tag{3.1}$$

$$R_{20s} = \frac{\Delta V_1}{\Delta I} = \frac{\mid V_1 - V_2 \mid}{\mid I \mid} \tag{3.2}$$

It is worth to mention here, that the time constant involved from V1 to V2, as usually seen in electrical engineering, is characterized by a parallel RC circuit as shown in Figure 3.2 and this procedure is useful when parameterizing performance models as seen in [33]. The capacitance responsible for the time constant is determined in [34] by equation 3.3. However, performance modelling is out of the scope of this project, as here the main purpose is to extract the parameters of $R_{ohmic}$, $R_{20s}$, and $C_p$, in order to perform diagnostics through calendar ageing (SOH) and SOC and to evaluate pulse power capability.

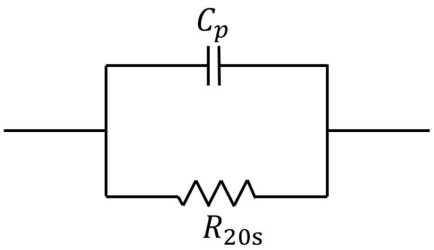


Figure 3.2: A typical RC circuit used to represent the transient voltage response

$$C_p = \frac{\tau}{R_{20s}} \tag{3.3}$$

Where, $\tau = -\frac{t}{ln(\frac{V_2}{V_1})}$, $R_{20}$ the resistance and t is the time from $V_1$ to $V_2$.

As presented in Section 2.5, the internal resistance depends on the SoC, the temperature, and the C-rate (load current). Thus, these conditions should be specified during the application of this method. In Figure 3.3 the dependence on the load current is presented with the voltage drop that varies accordingly, as investigated in [12]. While in Figure 3.4 the dependency on the pulse duration, the SOC and temperature is shown from dc impedance measurements that where analysed in [13].

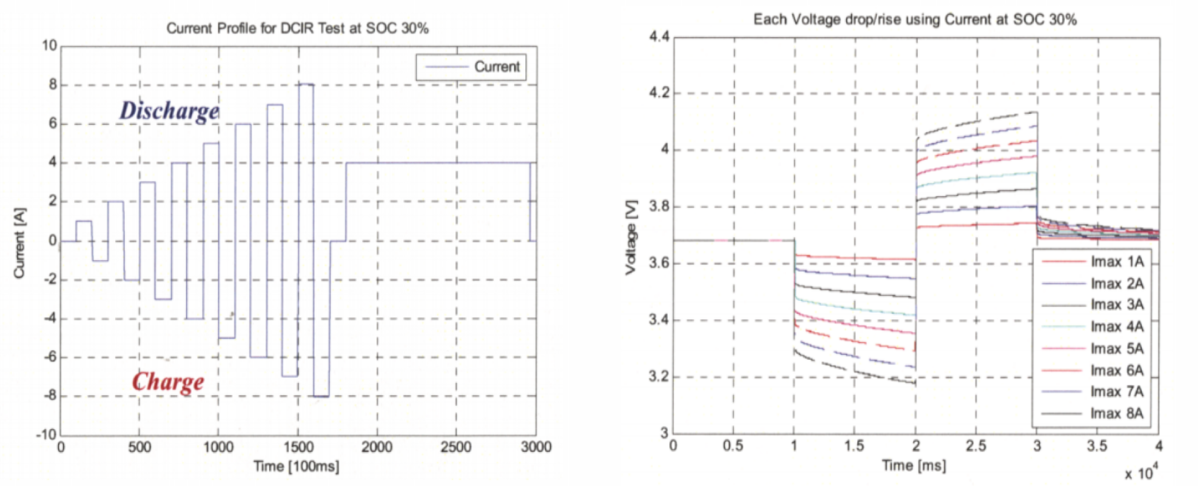


Figure 3.3: At 30% SOC: (Left) dc current pulses applied at different C-rates (Right) the voltage respond to both discharge and charge pulses applied [12]

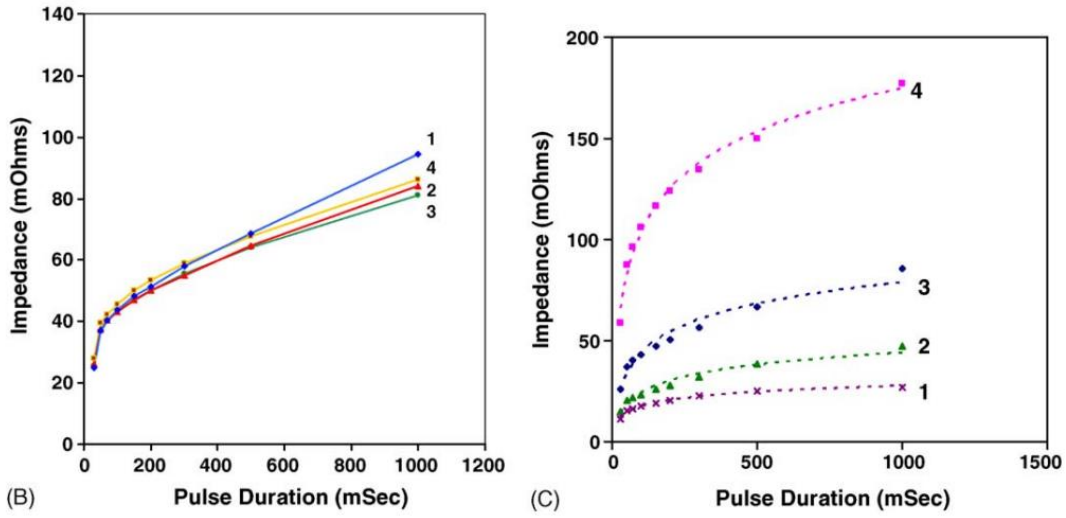


Figure 3.4: (Left) The increase of impedance along with pulse duration and SoC (1) 100% (2) 75% (3) 50% (4) 25%, and (Right) at different temperatures (1) 20 °C (2) 0 °C (3) −20 °C (4)−30 °C [13]

## 3.2 Electrochemical Impedance Spectroscopy (EIS)

The Electrochemical Impedance Spectroscopy, is a commonly used method to determine the AC impedance of batteries. This method enables the measurement of the reactive components that ac impedance involves such as the inductive and capacitive behaviours that batteries exhibit and that are frequency dependant as seen in equation 3.4 and equation 3.5.

$$X_L = j\omega L \tag{3.4}$$

$$X_C = \frac{1}{j\omega C} \tag{3.5}$$

According to [35] the measurement principle is to apply sinusoidal excitation signals of small amplitude and of different frequency, to a tested cell. The response to this repetitive input signal, is limited by the ac impedance that the battery exhibits and a different time phase shift is encountered each time the signal is applied. A time phase shift is illustrated in Figure3.5 (Left) where voltage is assumed to be the response limited by impedance to an input sinusoidal current. Impedance $Z$ as a complex number is better represented in the Nyquist plane as illustrated in Figure 3.5 (Right), where the y-axis facilitates the frequency dependant reactance.

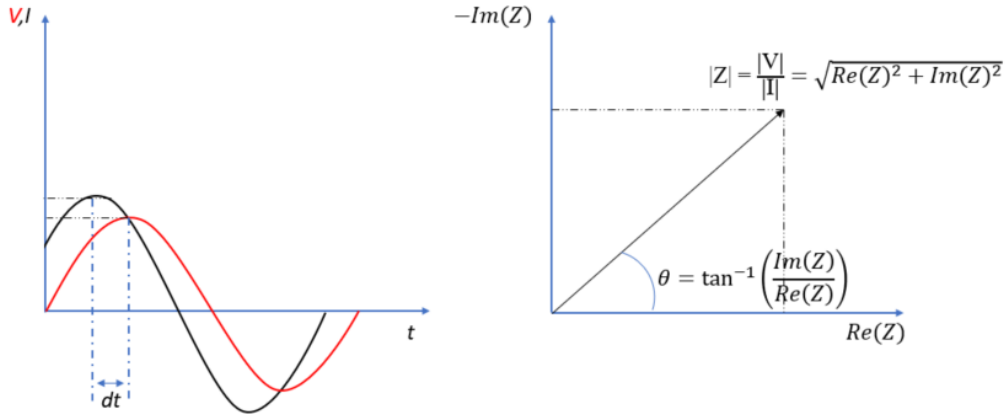


Figure 3.5: (Left) The time phase shift due to impedance measured between the voltage response and the sinusoidal excitation current input. (Right) The representation of complex impedance consisted of the impedance magnitude and phase shift in degrees

It is worth to mention here, that when voltage is the measured response, the measurement is referred to as galvanostatic mode and when current is the measured response it is the potentiostatic mode [14]. In galvanostatic mode the input and output signals are presented in equation 3.6 and equation 3.7 while the transfer function of impedance is expressed in equation 3.8.

$$Input : \Delta I = Imax \cdot sin(2\pi ft) \tag{3.6}$$

$$Output : \Delta V = Vmax \cdot sin(2\pi ft + \theta) \tag{3.7}$$

$$Z(j\omega) = \frac{Y(j\omega)}{U(j\omega)} = \frac{Output\Delta V}{Input\Delta I} \tag{3.8}$$

The polar and exponential forms in which impedance is also expressed through the literature are shown in equation 3.9 and equation 3.10.

$$Z = \frac{\mid V \mid}{\mid I \mid} \angle \theta V - \theta I \tag{3.9}$$

$$Z = \frac{\mid V \mid}{\mid I \mid} e^{j(\theta V - \theta I)} \tag{3.10}$$

Where, $\frac{|V|}{|I|} = \mid Z \mid = \sqrt{Re(Z)^2 + lm(Z)^2}$, and $(\theta V - \theta I) = \theta = tan^{-1}\left(\frac{lm(Z)}{Re(Z)}\right)$

The impedance characteristic which is also referred to as impedance spectra in the literature, is illustrated in Figure 3.6 (left), and is usually presented through the Nyquist plane, starting with the minimum frequency on the right. One of the main advantages of EIS, is that the impedance curve allows the interpretation of a battery's behaviour at various frequencies with the use of the resistive and reactive impedance parameters [14]. Moreover, a state-of- the-art electrical equivalent circuit (EEC) shown also in Figure 3.6(right) is commonly used to model and fit the curve, as each EEC element is associated with a corresponding region. This procedure is presented analytically in the next chapter where the EIS is applied.

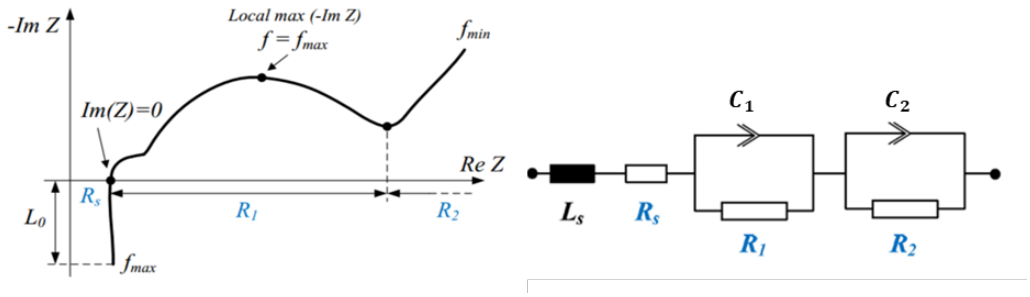


Figure 3.6: Typical Impedance spectrum and an EEC impedance model for utilizing the extracted impedance parameters: inductive parameter from the maximum frequency, Rs from the intersection with Real(Z) axis, R1 from distance of Rs till local min, C1 from local max, and C2 from minimum frequency [14]

From this process each impedance parameter can be extracted and evaluated according to the obtained values at different internal and external conditions as SOC, age, and various temperatures. In Figure 3.7 from [15] the lowest temperatures show to exhibit higher impedance at lower frequencies, while in Figure 3.8 the dependency on ageing is shown by the investigation done in [5].

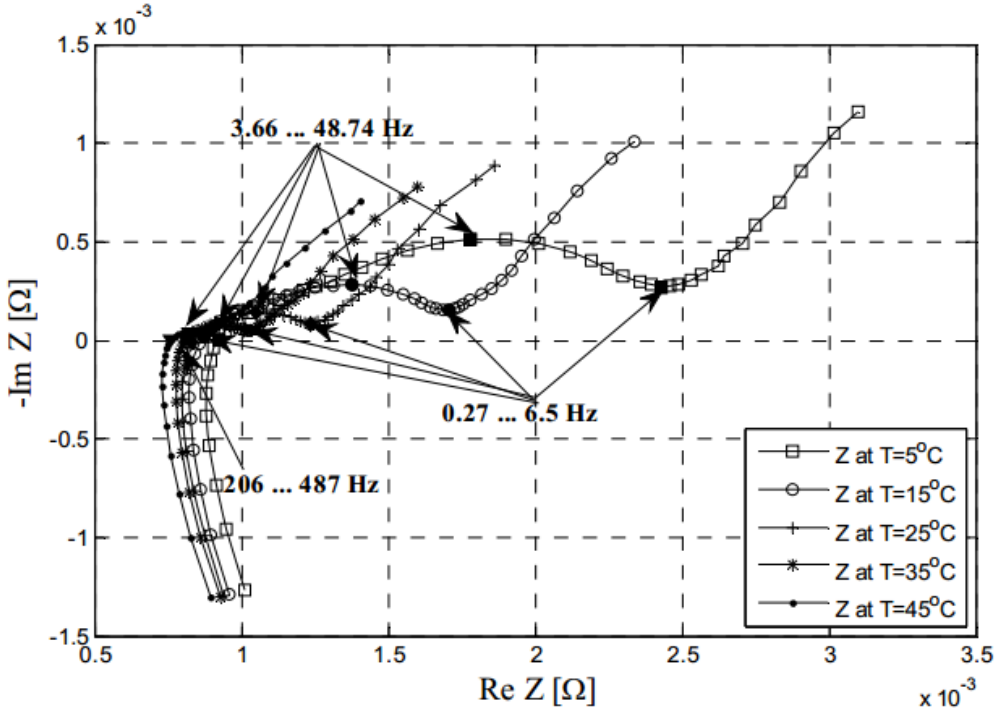


Figure 3.7: Change of impedance spectra from a LTO battery at various temperature conditions and stable 50% SOC [15]

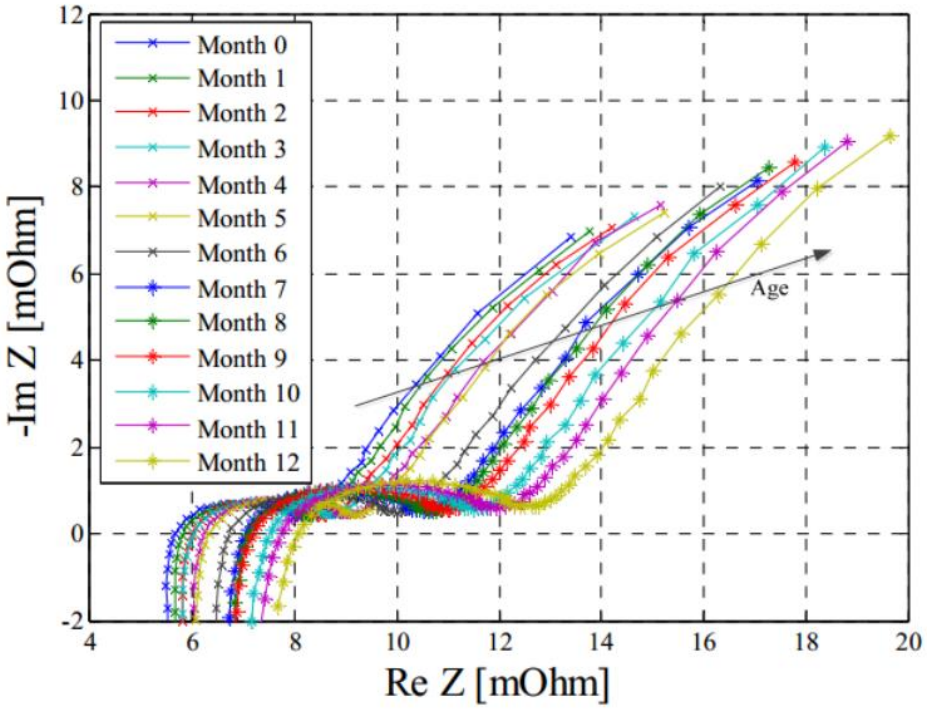


Figure 3.8: The ageing effect on the total impedance spectra of an LFP cell after accelerated lifetime test in [5]

## 3.3 Pseudo Random Binary Sequence (PRBS)

In this section, an introduction to the fundamental concept of pseudorandom binary sequence signals (PRBS) is presented, which is a type of square wave but of random sequence. PRBS is used in many fields such as in telecommunication engineering, identification procedures of photovoltaic systems [36], battery parameter identification on which SOH estimations would be possible [37], and impedance measurements for the purpose of battery diagnostics in [16] as seen in Figure 3.9. The main advantage of PRBS compared to the EIS according to [37], is that the application of this method can be performed online and does not require the battery to be disconnected from the load.

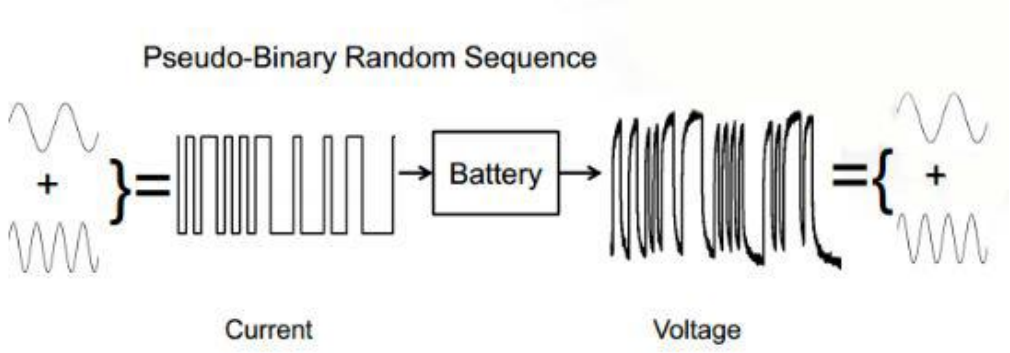


Figure 3.9: PRBS application on a battery used to obtain impedance measurements [16]

The PRBS generator is designed by linear feedback shift registers (LSFR) and a logic operator XOR as seen in Figure3.10 where a 12-bit PRBS is presented as an example. Also, a part of the generated signal that exhibits the random sequence described above, is shown in Figure3.11.

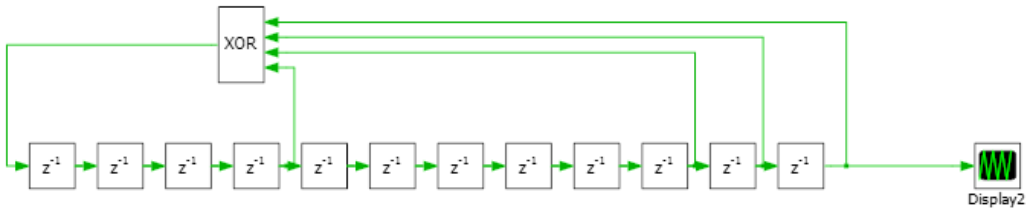


Figure 3.10: Illustration of a 12-bit PRBS

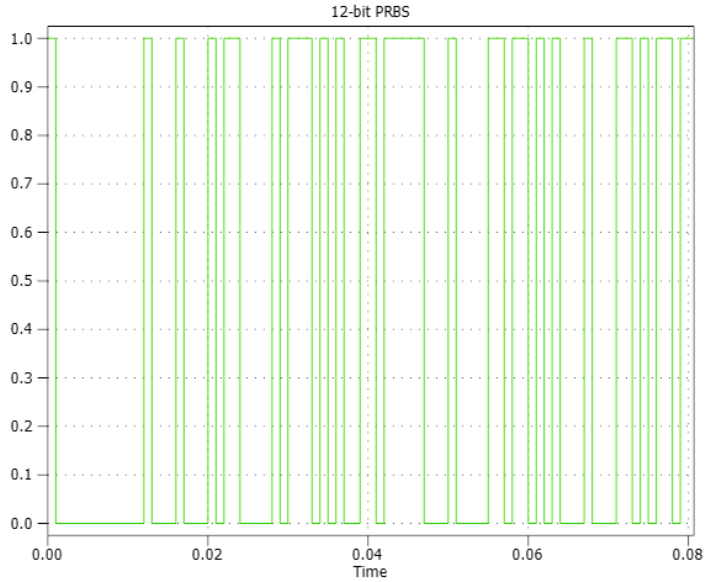


Figure 3.11: Part of the generated 12-bit PRBS signal

The main factors that determine the design of PRBS signals when a targeted frequency range ($f_{min}$ to $f_{min}$) is known, are listed below.

- The number of needed LSFRs which determine the number of bits
- The length N of the PRBS signal
- The clock frequency $f_c$ which is the shifting frequency for the LSFRs
- The bandwidth frequency $f_B$ which is the final maximum frequency that corresponds to $-3dB$ gain of the power spectral density

The length N of a PRBS signal is the number of states (0,1) it contains during a period and is determined by the number of bits n as shown in equation3.11

$$N = 2^n - 1 \tag{3.11}$$

However, when the number of bits is not known, the clock frequency is found through equation 3.12, and then the number of bits can be later found through equation 3.13. according to [38].

$$f_{max} = \frac{f_c}{3} \tag{3.12}$$

$$f_{min} = \frac{f_c}{N} \tag{3.13}$$

According to [38], when the design of the PRBS is completed, the Fast Fourier Transformation (FFT) is the mathematical tool requirred for the decomposition of the signal and the $f_{min}$

is the fundamental frequency based on which the FFT is performed. From this process, the useable frequency range is depicted through the power spectral density at $-3dB$ as shown in Figure3.12, and the maximum useable frequency is determined. This limit (3-dB) is claimed to be a rule of thumb in the literature and the methodology of obtaining the power spectral density. The procedure is presented analytically in [38]. After these computations the final information contained in the PRBS signal is:

$$f_{min} : f_{prbs} : f_{max}$$

Where $f_{prbs}$ is the frequency step of time period:

$$T_{prbs} = \frac{1}{f_{min}} \tag{3.14}$$

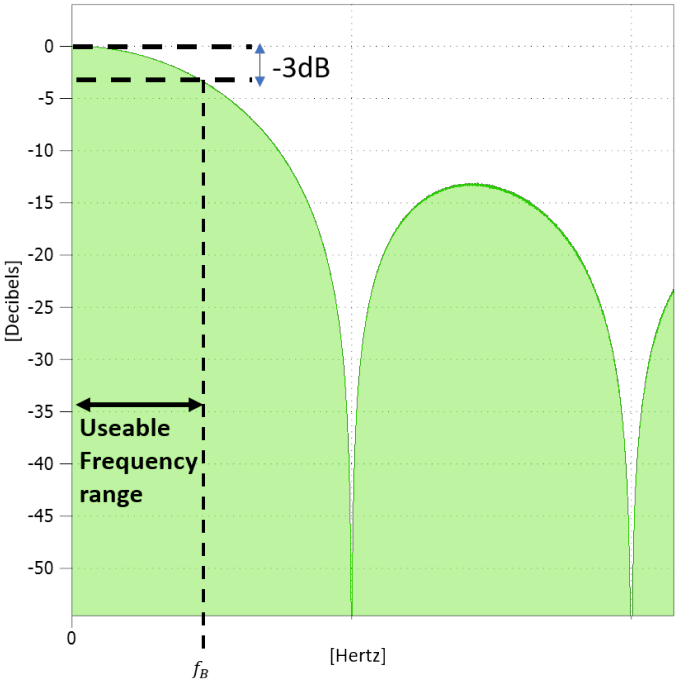


Figure 3.12: FFT of a 12-bit PRBS with the useable frequency range indicated

The impedance determination with the use of PRBS is investigated thoroughly in [37], and here in this project the simulation feasibility is demonstrated in Chapter 5

# Part II

# Implementation

# 4 | Reference Performance Tests (RPT)

In this chapter, an overview of the reference performance tests (RPT) that were conducted every month to measure the calendar ageing is presented. A Nickel Manganese Cobalt/Graphite (NMC) cell of 28Ah capacity was used, which is used also in EV applications and is shown in Figure 4.2 . As calendar ageing from BOL to EOL takes long time in real-life conditions, the degradation was achieved by accelerated ageing which is keeping the battery in storage under severe conditions such as constant high temperature. Specifically, in this project the cell was kept in a climate chamber during each month under 40°C which is considered high enough compared to usual operating temperature. Furthermore, the calendar ageing was performed by keeping the cell constantly at 90% SOC. In Figure 4.1 the monthly schedule of the RPT is shown with the order that every step was taken.

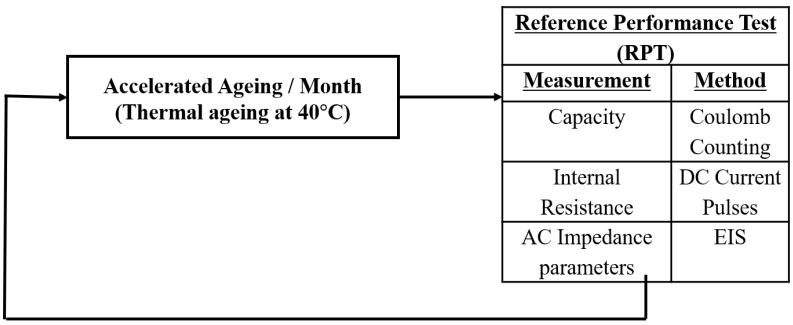


Figure 4.1: Schedule of reference performance tests


Figure 4.2: The tested NMC/graphite lithium ion pouch cell by Leclanche


Figure 4.3: The power supply and climate chamber used for the experiments

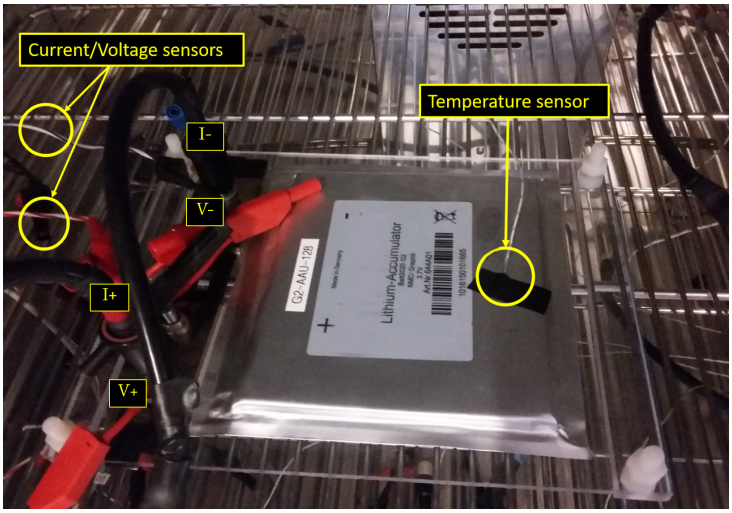


Figure 4.4: The sensors and power supply cables

## 4.1 Capacity Check

In this project, the capacity measurement was obtained after two cycles of charging and discharging the battery through the conventional method of CC-CV (constant current-constant voltage), and by taking into consideration the second amount of totally discharged capacity. During this process, since the capacity is unknown, the actions of full cycles were performed based on the maximum and minimum voltage limits that are usually provided in the battery specifications. This process was initiated by totally discharging the battery with constant current of 1C-rate which in this case is 28A until the minimum discharge voltage -for the tested NMC cell- of 3V was attained. After following a 1 hour resting period, constant charging of 1 C-rate was applied until the maximum charging voltage of 4.2V was attained. From this point, the constant voltage of 4.2V kept the charging process until the battery current reached C/20 (i.e., in this case 1.4 A). At that moment the battery was considered to be fully charged. Same as before, 1 hour for resting period was given and a full discharge of the battery with 1 C-rate constant current took place. The same procedure was followed once more and the capacity was checked during

the last total discharge with the use of equation 2.4. Below, Figure 4.5 and Figure 4.6 show the described procedure.

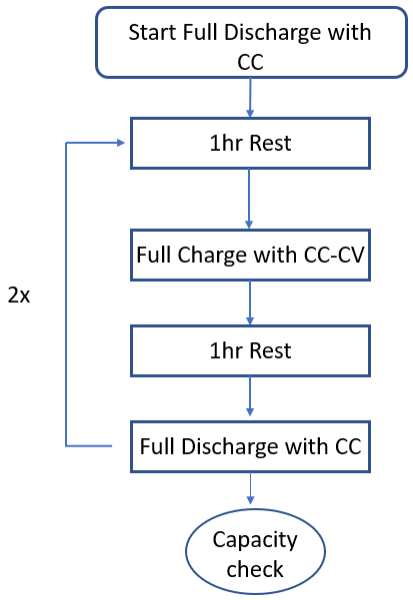


Figure 4.5: Capacity test schedule

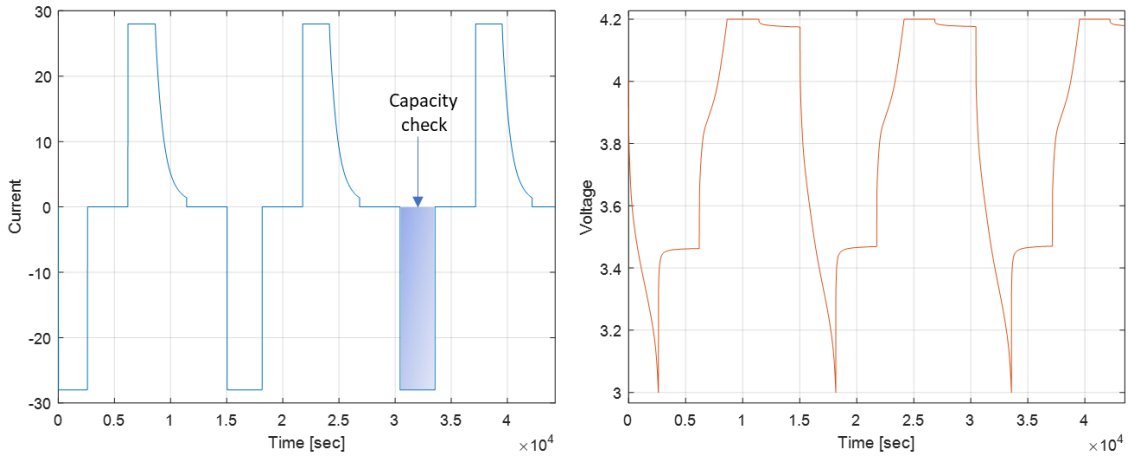


Figure 4.6: CC-CV charging method. (Left)Constant current charging and (Right) Constant voltage charging

### 4.1.1 Capacity Fade

After each month of calendar ageing (accelerated), the capacity was measured by following the described procedure in previous section while, capacity fade was computed with the use of the following expression in equation 4.1. The results are presented in table 4.1 and illustrated as normalized values based on the BOL condition in Figure 4.7, while the resulting SOH condition

in terms of capacity and EV aplications are listed in table 4.2.

$$Q_{Fade}[\%] = \frac{Q_{BOL} - Q_{measured}}{Q_{BOL}} \times 100 \tag{4.1}$$

As seen, after the first 30 days of accelerated calendar ageing there is no substantial capacity fade, however after 90 and 120 days the fading effect is significant reaching between 7-8% at the last monthly capacity check. It is important to mention here that the measurements after 60 days are not presented due to an erroneous measurement. The capacity fade was measured too high and was not reasonable to exploit the result as it wasn't matching to previous and later results.

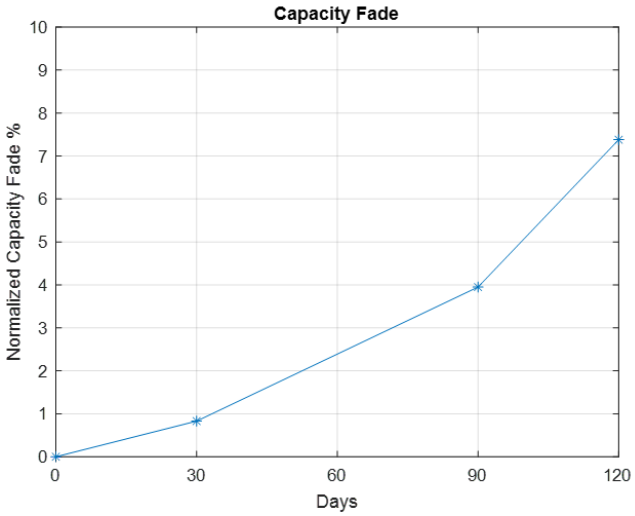


Figure 4.7: Normalized capacity fade based on the BOL condition

| | **Capacity [Ah]** | **Capacity Fade** |
|---|---|---|
| **BOL** | 24.4295 | 0% |
| **30 days** | 24.2277 | 0.83% |
| **90 days** | 23.4654 | 3.95% |
| **120 days** | 22.6254 | 7.38% |

Table 4.1: Results of capacity fade measurements

| **Age** | $SOH_Q$ | $SOH_{EV}$ |
|---|---|---|
| **BOL** | 100% | 100% |
| **30 days** | 99.72% | 95.87% |
| **90 days** | 96.05% | 80.26% |
| **120 days** | 92.62% | 63.07% |

Table 4.2: The resulting SOH in terms of capacity and EV applications

## 4.2 Application of DC Current Pulses

For the diagnosis of internal resistance increase during the accelerated calendar ageing, the DC current pulse technique was first applied, and measurements were taken through the current injection method as shown in Figure 4.8(Left) where the voltage responds are illustrated as well Figure 4.8(Right). This test was performed every month in a similar manner after every capacity check, in order to obtain updated measurements of the resistance at 80%, 50% and 20% SOC for each case. Discharging the battery was achieved by applying constant current of 1 C-rate amplitude until the desired SOC levels was reached. At each SOC level, the applied pulses of charge and discharge lasted for 20 seconds with an intermediate resting time of 15minutes between each other.

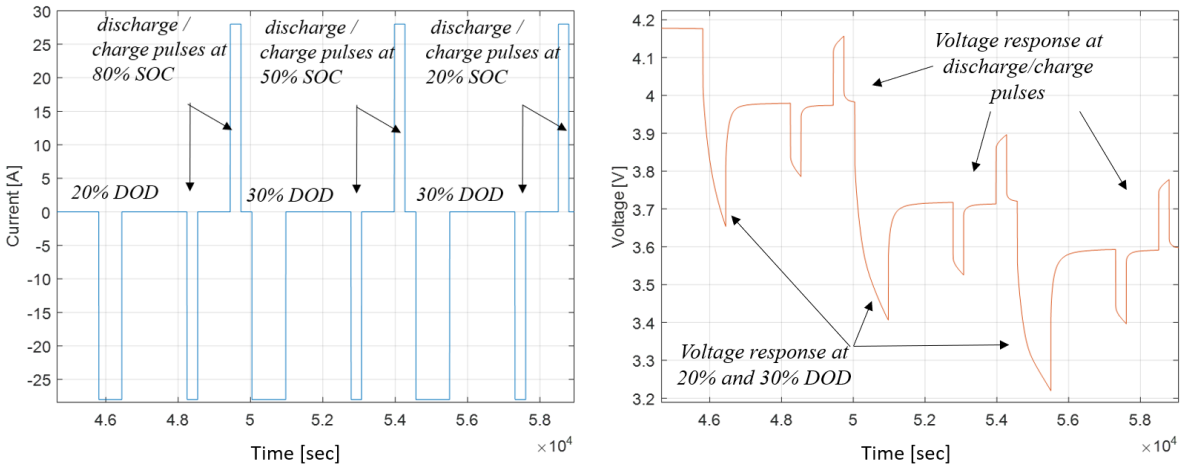


Figure 4.8: Illustration of the applied CC discharge before each discharge/charge pulse

Afterwards, as shown in Figure 4.9, the two resistances described in section 3.1 where determined by the voltage respond during discharge and charge pulses of 1 C-rate, and the measurements where done by taking into account two sequential time intervals. The resistance due to pure ohmic effect $R_{ohmic}$ , which is assumed to take place during the instantaneous voltage change, is determined in the range of 0-0.1 seconds. From this point and further, the voltage respond that contains a longer time constant, from $V_1$ to $V_2$, is where the $R_{20}$ is determined and represents the resistance by charge transfer and diffusion polarization effects. The aim of this analysis is to make a conclusion regarding the trends that each resistance follows, but also the contribution of each to the internal resistance increase. In table 4.3 the absolute values of the decomposed internal resistance are presented as they were measured at BOL.

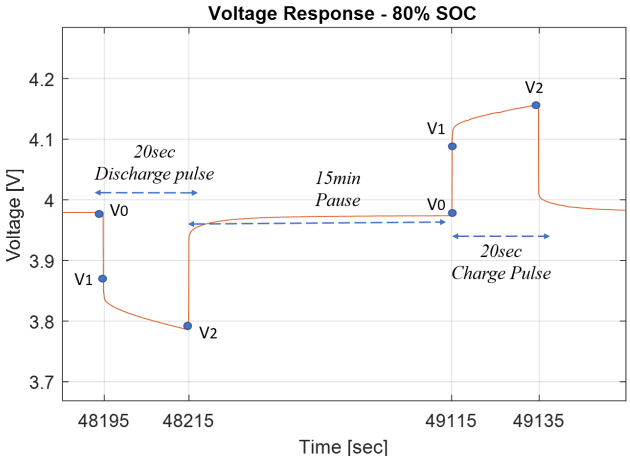


Figure 4.9: The voltage response at discharge and charge pulse and the points of interest for determining the pure ohmic and charge transfer resistances

| **Discharge** | | |
|---|---|---|
| **SOC** | $R_{Ohmic}$ **[mOhm]** | $R_{20s}$ **[mOhm]** |
| **80%** | 4.0 | 2.2 |
| **50%** | 4.1 | 2.0 |
| **20%** | 4.3 | 2.3 |
| **Charge** | | |
| **SOC** | $R_{Ohmic}$ **[mOhm]** | $R_{20s}$ **[mOhm]** |
| **80%** | 4.1 | 1.8 |
| **50%** | 4.2 | 1.7 |
| **20%** | 4.4 | 1.9 |

Table 4.3: Absolute values of decomposed internal resistance at BOL

In Figure 4.10 the ohmic resistance $R_{ohmic}$ is illustrated and a certain trend of increasing after every monthly measurement is noticed during the calendar ageing. However, some small deviations are noticed between the three analysed SOC levels. Specifically, it can be seen in Figure4.10 (top left), during 80% SOC, there is a steady increase after every monthly measurement, starting from 12% for both charge and discharge $R_{ohmic}$. After 90 days the increase has reached between 25-30%, and finally at the last measurement after 120 days, both charge and discharge $R_{ohmic}$ are measured 36-40% above from BOL regarding 80Q% SOC. At 50% SOC, Figure 4.10 (top right), the trend of $R_{ohmic}$ increase is almost identical to the 80% SOC as the measurements during both charge and discharge pulses are seen in the same range. Finally, at 20% SOC, Figure 4.10 (bottom), the same tendency of increasing $R_{ohmic}$ is seen during both charge and discharge pulses, however, after the 90 day measurement, this SOC level seems to increase 5-10% less than the higher SOC levels.

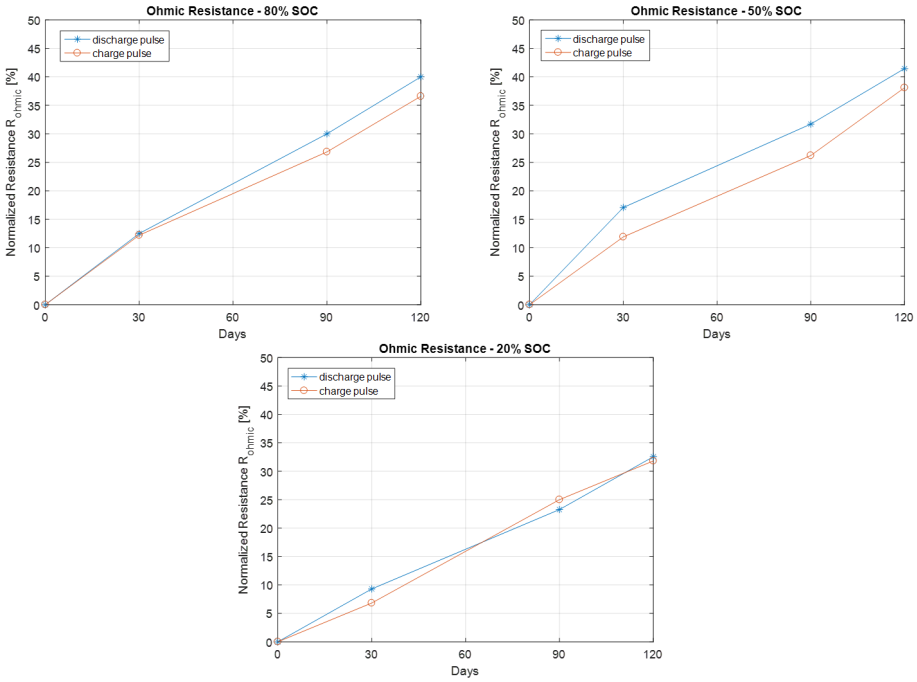


Figure 4.10: Illustration of the ohmic resistance during charge and discharge pulse for (Top Left) 80% SOC, (Top Right) 50% SOC, (Bottom) 20% SOC

In Figure 4.11 the charge transfer and diffusion polarization resistance $R_{20s}$ is illustrated and same as the ohmic resistance, an increasing trend is noticed as well. However, the final increase is seen to be much less compared to $R_{ohmic}$ at all SOC levels. By analysing separately each case, it can be seen in Figure 4.11 (top left), that after the first 30 days, both the charge and discharge $R_{20s}$ at 80% SOC, increase between 8-10%. After 90 days this increasing trend has continued and the charge $R_{20s}$ is seen to increased even more than 20%. However, at the last measurement after 120 days, this trend is stabilized and both charge and discharge resistance remained at the same trend slightly above 20%. At 50% SOC that is seen in Figure 4.11 (top right), after the first 30 days, only the charge $R_{20s}$ increased over 10%, while the discharge $R_{20s}$ remained at its initial value. However, after 90 days, the discharge $R_{20s}$ nearly compensated and during this measurement both charge and discharge $R_{20}$ increased between 15-20%. This trend remained the same even after 120 days. At 20% SOC that is seen in Figure 4.11 (bottom), after 30 days, the same trend was followed as in 50% SOC, the discharge $R_{20s}$ showed no change compared to its initial value but the charge $R_{20s}$ increased less than 10%. At the end however, both showed the less increase from all cases, between 5-10%.

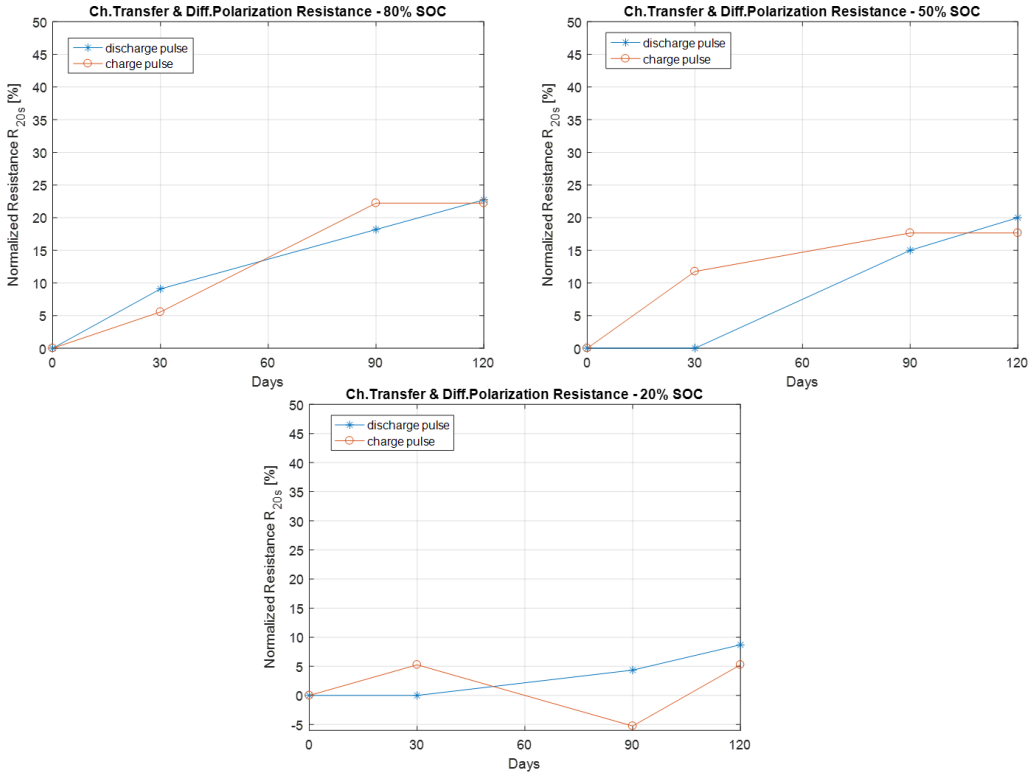


Figure 4.11: Illustration of the charge transfer resistance during charge and discharge pulse for (Top Left) 80% SOC, (Top Right) 50% SOC, (Bottom) 20% SOC

In Figure 4.12 the variation of the capacitance that is associated with the time constant of charge transfer is shown, as this parameter is decreasing with calendar ageing. At 80% SOC Figure 4.12 (top left), during both charge and discharge pulse, a significant decrease is noticed after the final measurement that reaches a 35% normalized value compared to BOL. It is an interesting fact that in earlier stages, during the charge pulse, there is no significant trend in the first 30 days, however after 90 days the final decrease is already achieved. At 50% SOC Figure 4.12 (top right), it is seen that after 30 days of calendar ageing there is no significant decrease during the discharge pulse but more than 10% during the charge pulse. After 90 days of calendar ageing, for both pulses the trend is the same and reaches a 25% decrease. Finally after 120 days calendar ageing, the capacitance decrease was measured at 25% and 30% for discharge and charge pulse respectively. At 20% SOC Figure 4.12 (bottom), after 30 days calendar ageing during both charge and discharge pulses the capacitance decrease is seen at 10% and 20% respectively. After 90 days both decrease by 10% and finally after 120 days, for the discharge pulse capacitance, the decrease is seen between 15 to 20% while for the charge pulse the decrease, between 25 to 30%.

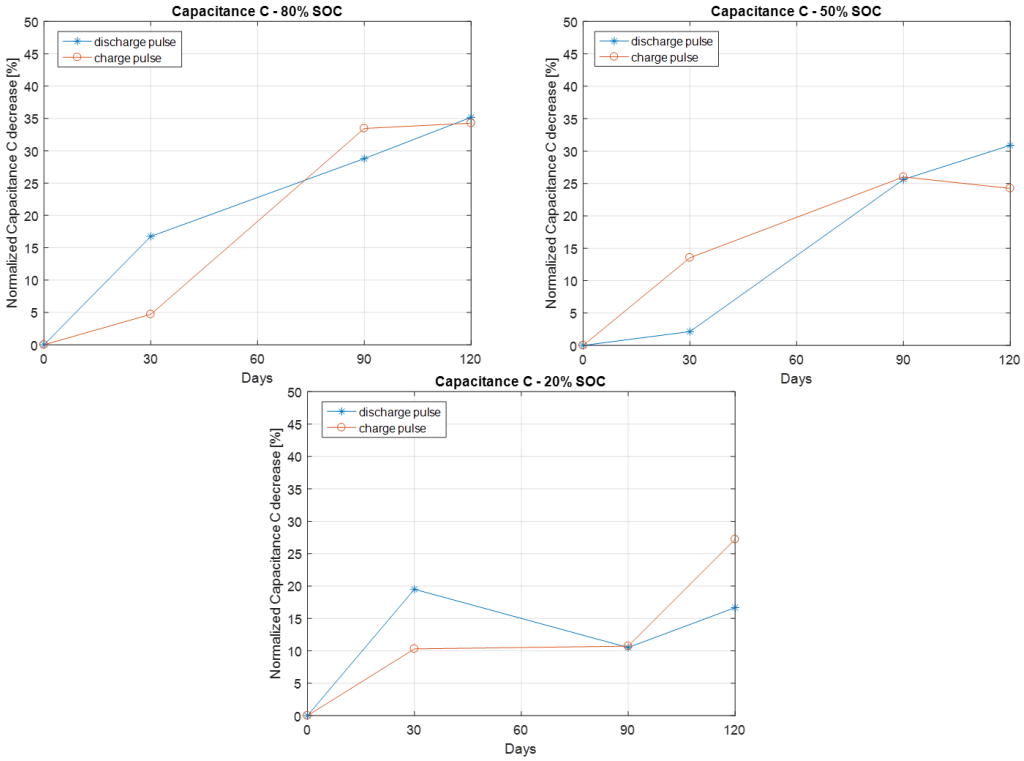


Figure 4.12: Illustration of the capacitance associated with charge transfer resistance during charge and discharge pulse for (Top Left) 80% SOC, (Top Right) 50% SOC, (Bottom) 20% SOC

### 4.2.1 Pulse Power Capability

In Figure 4.13, the results of pulse power capability (PPC) are presented as normalised values based on BOL condition. The computations where performed by following equations 2.7 and 2.8 and as seen the power fade is not substantial, thus in terms of PPC the tested cell is considered to be not aged enough. More specifically, in Figure 4.13 (top left), at 80% SOC at the final measurement during discharge pulse the decrease is approximately 2%. During charge pulse the PPC showed an increase of approximately 3%. In Figure 4.13 (top right) and (bottom), the 50% SOC and 20% SOC show a very similar evolution during both discharge and charge pulses. During discharge the PPC decrease is seen around 3% after the last calculation at 120 days, while during charge pulses an increase once again is seen for less than 2%.

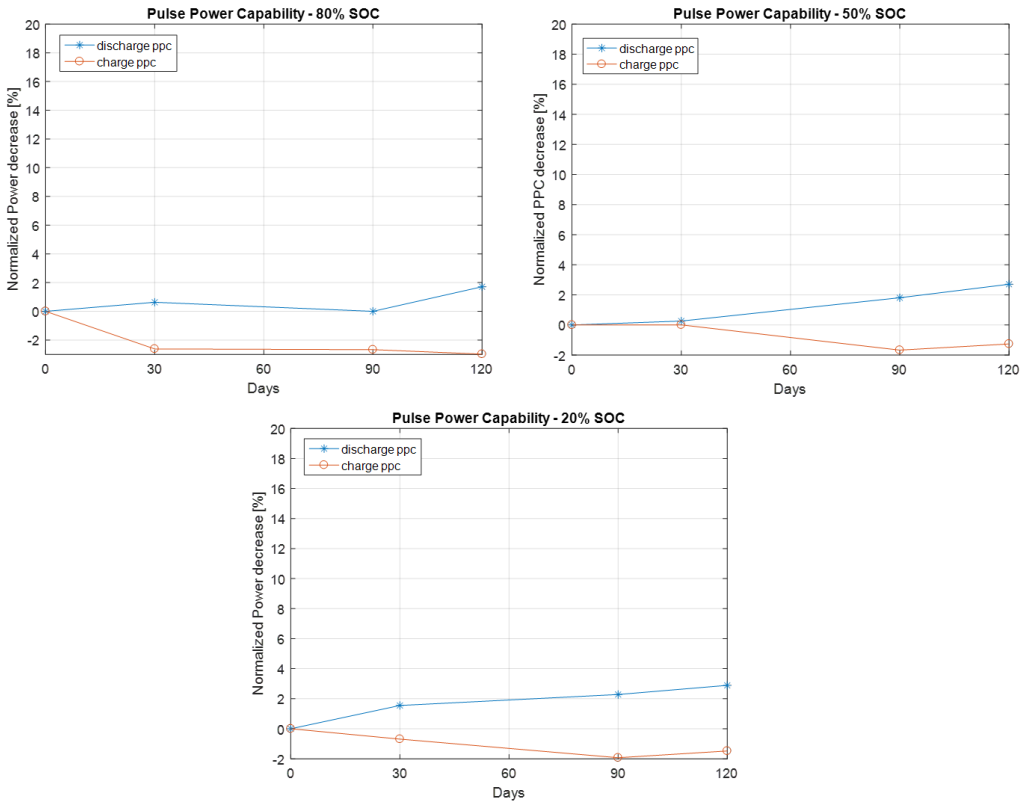


Figure 4.13: Illustration of the pulse power capability during charge and discharge pulse for (Top Left) 80% SOC, (Top Right) 50% SOC, (Bottom) 20% SOC

### 4.2.2 Summary

Overall, as a conclusion with regards to the DC current pulses, the decomposed resistances $R_{ohmic}$ and $R_{20s}$ were monitored along with calendar ageing and the $R_{ohmic}$ gained most of the attention as the increasing trend was more significant than $R_{20s}$. Moreover, the dependecy on SOC was also possible to evaluate and it is seen that $R_{ohmic}$ shows the most increase at all investigated ages at 50% SOC, and the lowest at 20% SOC. Last parameter of the decomposed internal resistance was the capacitance $C$ associated with the $R_{20s}$ that was analysed as additional data that can be obtained from this method and useful for performance modelling which is out of the scope though. Furthermore the total internal resistance during the charge and discharge pulse was employed to measure the pulse power capability of each pulse. From this measurement it was seen that the performed ageing was not enough to observe a substantial change in terms of power capability. In other words, even though capacity has faded as seen from the capacity check measurements, this did not influence the power capability.

## 4.3 Application of Electrochemical Impedance Spectroscopy (EIS)

The process for obtaining the complex impedance value of the tested cell at the tested frequency range (0.010 – 10000Hz), was performed in galvanostatic mode according to section 3.2 description. When the impedance measurement was plotted in each SOC level, the characteristic shaped from the maximum to the minimum frequency was divided into regions as shown in Figure 4.14 and with the use of an EEC these parameters were extracted as also shown. In the highest frequencies starting from 10kHz, region 1 is defined to determine the inductive element. Region 2 defines the intercept with the real axis that is used to determine the pure ohmic resistance because at that point capacitive and inductive effects are not present and imaginary part is zero. The next regions 3,4,5, are used to define the resistive and capacitive behaviour due to the solid electrolyte interface (SEI) growth, charge transfer effects, and diffusion polarization processes. The frequency range in which the impedance EEC parameters were identified in this project are listed in detail in table 4.4 while the frequency borders between the defined ranges are depicted in Figure 4.14.

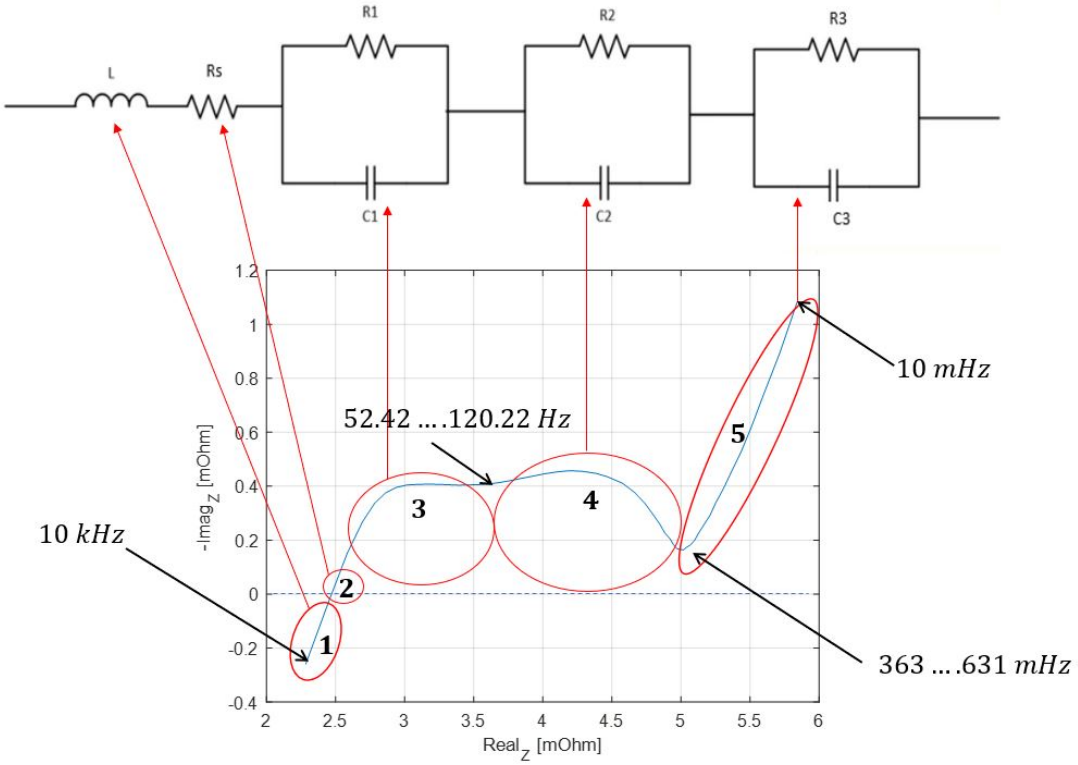


Figure 4.14: EEC impedance model and corresponding elements to specific ranges of the spectrum

| Region | EEC component | Origin | Frequency Range |
|---|---|---|---|
| **1** | $L_s$ | Inductive behaviour | 10 kHz-2.5119 kHz |
| **2** | $R_s$ | Ohmic resistance | 7.5 kHz-2.5119 kHz |
| **3** | $R_1//C_1$ | SEI growth | 2.5119 kHz-52.48 Hz |
| **4** | $R_2//C_2$ | Charge transfer | 120.22 Hz-363 mHz |
| **5** | $R_3//C_3$ | Diffusion polarization | 631 mHz-10 mHz |

Table 4.4: Impedance parameters that constitute the impedance model and the corresponding frequency range that each component corresponds to

The impedance model expressed in equation 4.2 based on the EEC of Figure 4.14 was used to perform the curve fitting. This procedure is important, because a well-tuned model that would fit the actual impedance spectra with the least possible error, would enable the determination of the closest value for each considered impedance parameter. Thus, the degradation of each component is possible to be monitored, as this is done repeatedly through the battery's lifetime.

$$Z = j\omega L + R_s + \left(\frac{R_1}{j\omega C_1 R_1 + 1}\right) + \left(\frac{R_2}{j\omega C_2 R_2 + 1}\right) + \left(\frac{R_3}{j\omega C_3 R_3 + 1}\right) \tag{4.2}$$

The error estimation was computed with the use of the normalized root mean square error algorithm (NRMSE) according to [39] as expressed in equation 4.2 and equation 4.3 for both Real and Imaginary axis and finally taking into account the average error.

$$NRMSE_{Real} = \frac{RMSE_{Real}}{max(Real_{actual}) - min(Real_{actual})} \tag{4.3}$$

$$NRMSE_{lmag} = \frac{RMSE_{Imag}}{max(Imag_{actual}) - min(Imag_{actual})} \tag{4.4}$$

Where, $RMSE_{Real} = \sqrt{\sum \frac{(Real_{model} - Real_{actual})^2}{N}}$

and $RMSE_{Imag} = \sqrt{\sum \frac{(Imag_{model} - Imag_{actual})^2}{N}}$

In Figure 4.15, the curve fitting that was performed by the derived model is illustrated for BOL, while the initial values for each parameter at the investigated SOC levels are presented in table 4.5 condition and is compared with the actual impedance measurements. All the fitting models and results that where plotted along with the corresponding actual measurements are shown in Appendix A.

| **EIS Impedance Parameters** | **80% SOC** | **50% SOC** | **20% SOC** |
|---|---|---|---|
| $L$ | 1.1152e-08 | 1.038e-08 | 9.936e-09 |
| $R_s$ | 2.201e-03 | 2.202e-03 | 2.224e-03 |
| $R_1$ | 0.758e-03 | 0.7947e-03 | 0.974e-3 |
| $C_1$ | 0.5013 | 0.4318 | 0.3231 |
| $R_2$ | 0.88014e-03 | 0.904e-03 | 1.0987e-3 |
| $C_2$ | 14.2543 | 11.6438 | 10.4016 |
| $R_3$ | 1.705e-03 | 1.5e-03 | 1.4021e-03 |
| $C_3$ | 0.852e+04 | 0.75e+04 | 0.85e+04 |

Table 4.5: Extracted initial values of impedance parameters at BOL condition

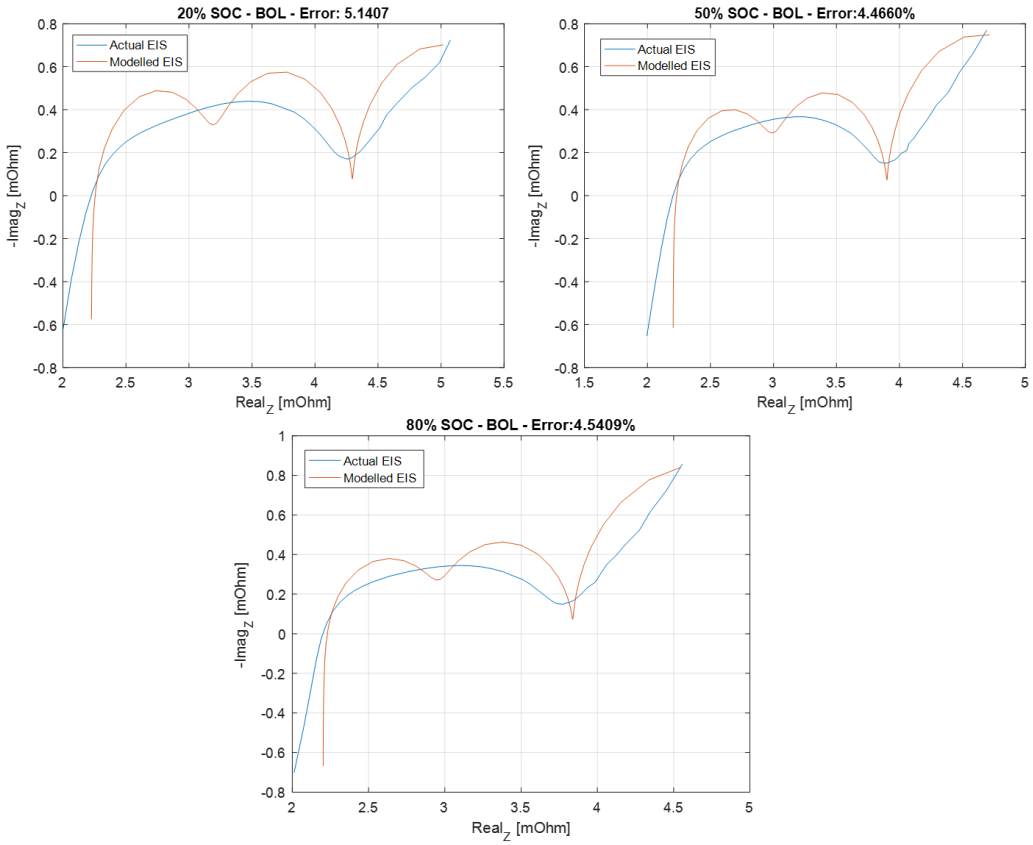


Figure 4.15: The EIS curve-fitting at BOL: (Top left) 20% SOC (Top right) 50% SOC (Bottom) 80% SOC

In Figure 4.16 the summary of the EIS measurements for the tested NMC cell are presented for each SOC level and some first observations regarding the overall impedance spectra could be drawn. After every monthly measurement, it can be seen that for all three SOC levels, a clear shifting is noticed in the low frequency range, in the same order with ageing. However the same trend is not seen in the high frequency regions where the tail and the intesept with real axis are following a random trend. These two first observations are shown in Figure 4.17 where the measurement of 80% SOC is used for the illustration. Furthermore, at all SOC levels, after the measurement of 60 days calendar ageing, it is obvious that the first semicircle shows a trend of growing amplitude which is assumed to be caused by the growth of SEI.

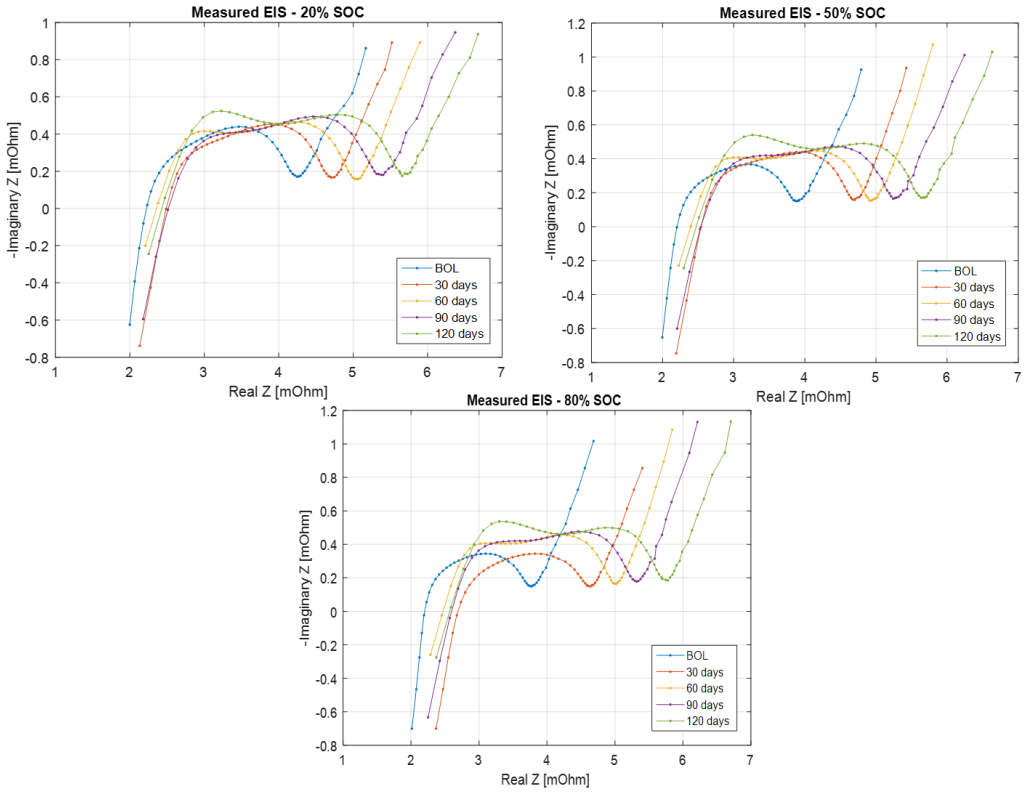


Figure 4.16: Overall impedance measurements for (top left) 20% SOC (top right) 50% SOC and (bottom) 80% SOC

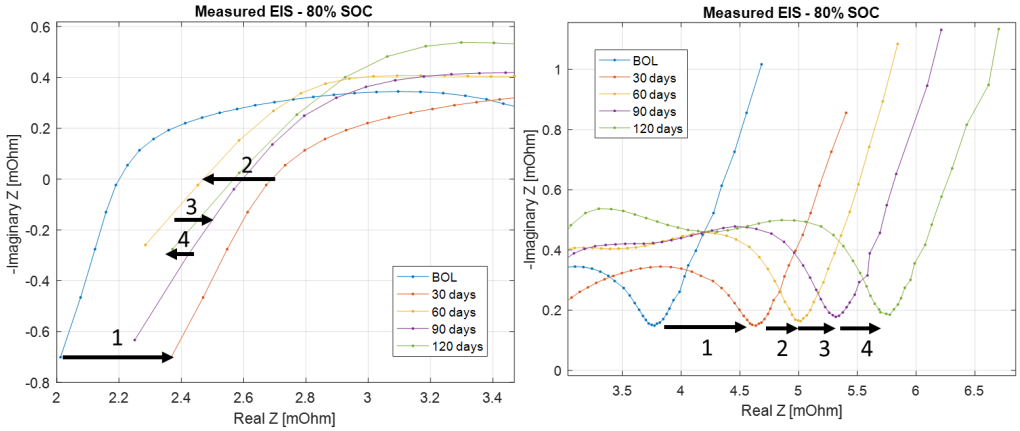


Figure 4.17: (Left) The shifting order in high frequencies and (Right) low frequencies

Another interesting perspective to analyse the measurements is shown in Figure 4.18, where the two extreme cases of BOL and last measurements after 120 days are compared based on SOC. As seen, at BOL, the 20% SOC has a large deviation from the other SOC levels, while after 120 days, the other SOC levels have compensated the difference and seem to nearly align each other.

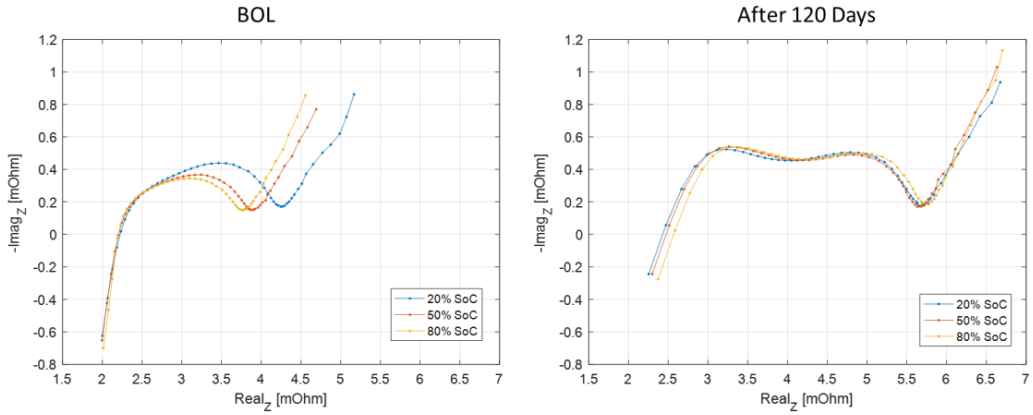


Figure 4.18: Comparison of SOC levels (Left) at BOL (Right) after 120 days

This difference which is later compensated by 50% SOC and 80% SOC can be seen in terms of total resistance which is expressed in equation4.5. In Figure 4.19 , the total resistance shows a trend to increase more for 80% SOC and 50% SOC but less for 20% SOC. This dependency on SOC is consistently valid through all calendar ageing measurements as seen.

$$R_{total} = R_s + R_1 + R_2 + R_3 \tag{4.5}$$

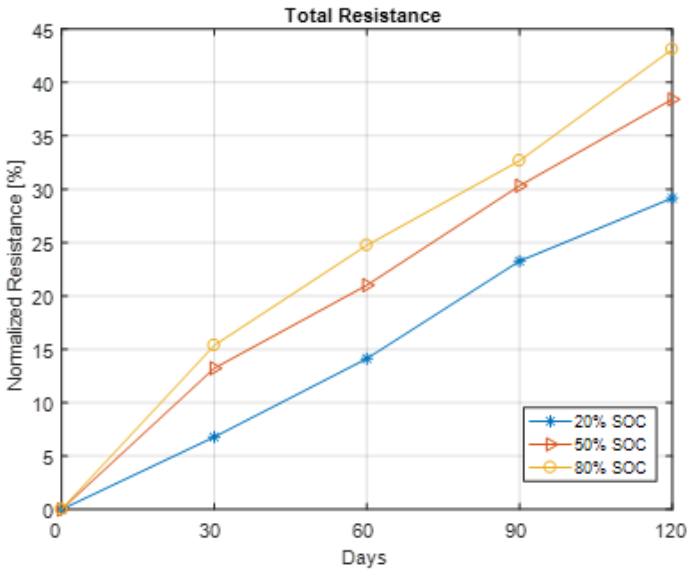


Figure 4.19: Normalized Total Resistance from EIS measurements for 20%, 50% and 80% SOC

### 4.3.1 Analysis of Extracted Impedance Parameters

At this point, the impedance parameters will be analysed separately to present each individual evolution and contribution to the overall impedance increase. In Figure 4.20, the normalized decrease of the EEC inductive element is presented first, and a fluctuating condition around 30% is noticed for all SOC levels. As seen, the most significant decrease is noticed after 60 and 120 days of accelerated calendar ageing which is between 25% and 55%. This has an effect on

making the inductive tail in the high frequencies shorter in the overall impedance measurements as seen in previous Figure 4.16. However, the fact that at30 days and 90 days this trend is not followed, makes it easy to say that this parameters is not changing with calendar ageing, thus has no significant contribution to the total impedance increase demonstrated earlier.

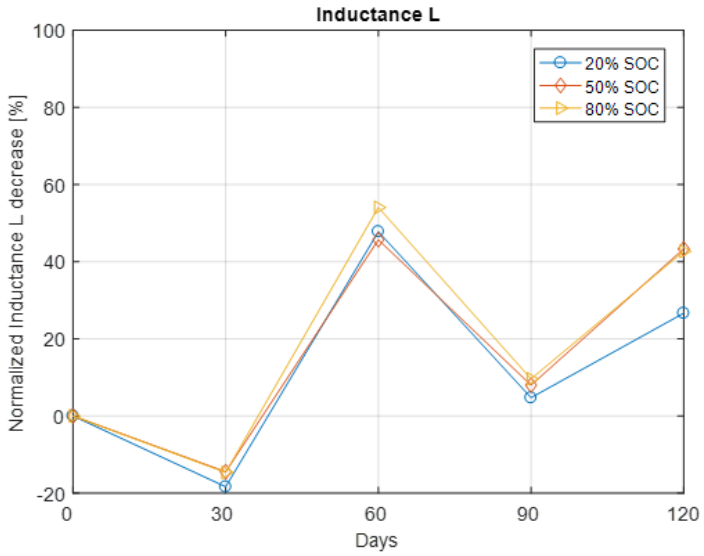


Figure 4.20: The normalized decrease of the EEC inductive element along with calendar ageing

In Figure 4.21, the normalized increase of the EEC ohmic resistive element $R_s$ is presented, and as for L, a fluctuating condition is noticed for all SOC levels, however in an increasing manner but not substantial. This fluctuating evolution at all SOC levels, is considered as the origin to the random shifting shown in Figure 4.17 (left) regarding the high frequency region. During all the measurements at 80% SOC the increase is noticed to be the highest and at 20% SOC the lowest. Thus, a dependency on SOC might be a conclusion but not on the performed calendar ageing (check this again).

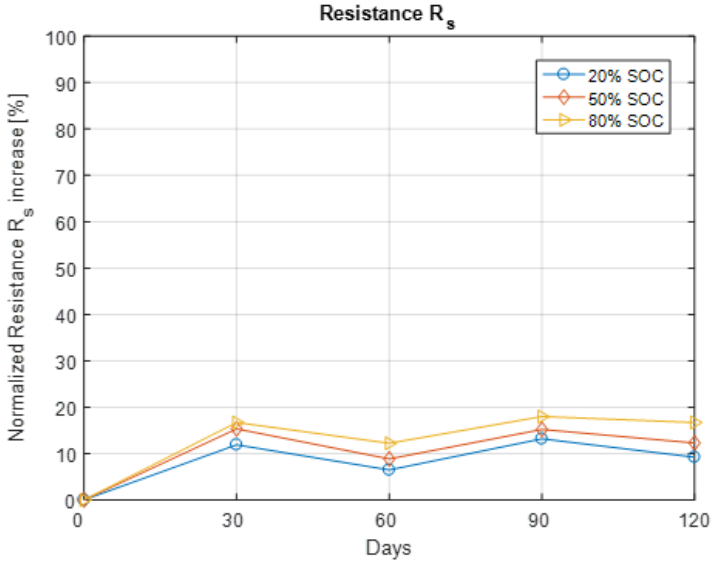


Figure 4.21: The normalized increase of the EEC ohmic resistance $R_s$

For both parameters L and $R_s$ ,due to the unstable evolution with calendar ageing, a conclusion

drawn is that there is no actual dependency on SOH that can be useful for diagnostics. In Figure 4.22, resistance $R_1$ and capacitance $C_1$ are presented together as they compose the first parallel RC circuit that is responsible for the first semicircle of the EIS spectra and subsequently the SEI growth. After every monthly measurement, $R_1$ has a consistent trend of increasing, and especially at 80% SOC, this increase is impressively almost 120% at the end of the performed calendar ageing. At 50% SOC a very similar trend is followed, while for 20% SOC, $R_1$ increases the less ( 75%), however still increasing consistently through the previous measurements. In Figure 4.23, this analysis is validated by illustrating the region that is related to the SEI growth for 80% and 20%. On the other hand, the capacitance associated with $R_1$ is seen to decrease rapidly between 70% and 80% for all 3 SOC levels until 60 days of calendar ageing where it maintains this condition even after 90 days. Finally this parameter after 120 days has increased for all studied SOC levels equally and approximately 85%.

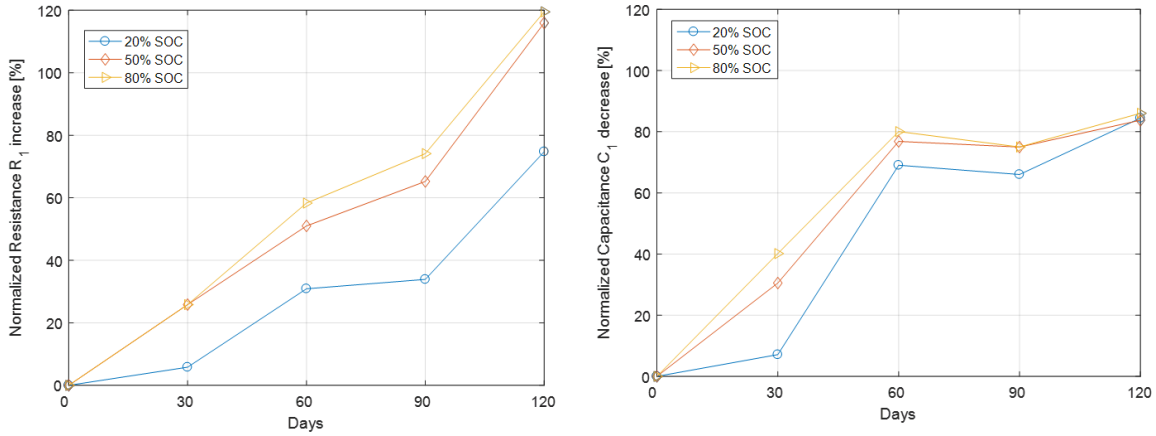


Figure 4.22: (left)Normalized increase of Resistance $R_1$ and (right)decrease of $C_1$ based on BOL

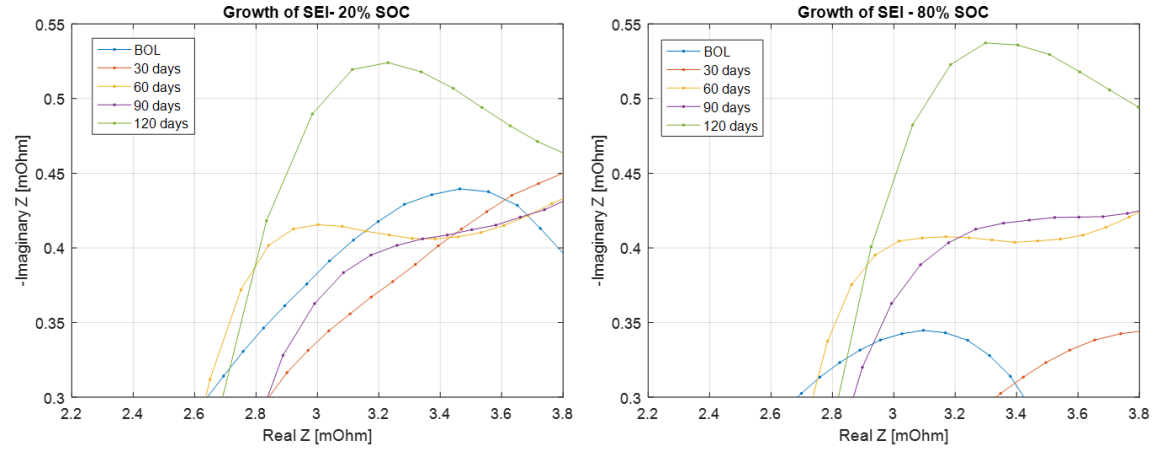


Figure 4.23: Close view of the region related to the SEI growth(left)20% SOC (right) 80% SOC

In Figure 4.24, resistance $R_2$ and capacitance $C_2$ that compose the second parallel RC circuit are shown, that are related to the charge transfer resistance and the double layer capacitance. From the first monthly measurement, it is seen that $R_2$ has a similar certain tendency to increase as previously $R_1$ . Moreover the same dependency on the SOC level is observed again until the final measurement, through all the calendar ageing as 80% SOC has the most increase, while 20% SOC has the least. However, in this case, after 60 days of calendar ageing the increase is taking place in a slower rate than $R_1$ but still is substantial as it finally increases between 40%

and 75% in the analysed SOC range. A similar trend is followed by $C_2$ , where the substantial increase based on BOL condition, is taking place with a spike noticed after 60 days. From that point, it seems to maintain an increase between 30% and 40% until the last measurement.

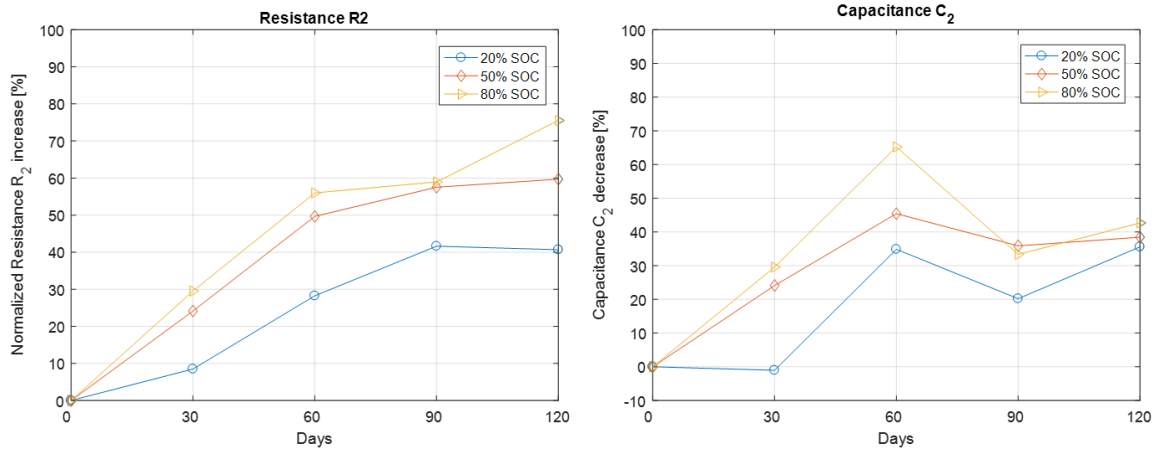


Figure 4.24: (left)Normalized increase of Resistance $R_2$ and (right) decrease of $C_2$ based on BOL

Finally, in Figure 4.25, resistance $R_3$ and capacitance $C_3$ are presented, that compose the third parallel RC circuit and are related to the polarization diffusion effects, and do not show any dependency on calendar ageing. The resistance $R_3$ fluctuates between 5% and 30% during the first measurements regarding all studied SOC levels, however at the final measurement an increase around 20% was observed for all analysed SOC levels. The capacitance on the other hand, which followed an unusual trend by increasing instead of decreasing finally was observed very close to the initial state when it was first measured at BOL.

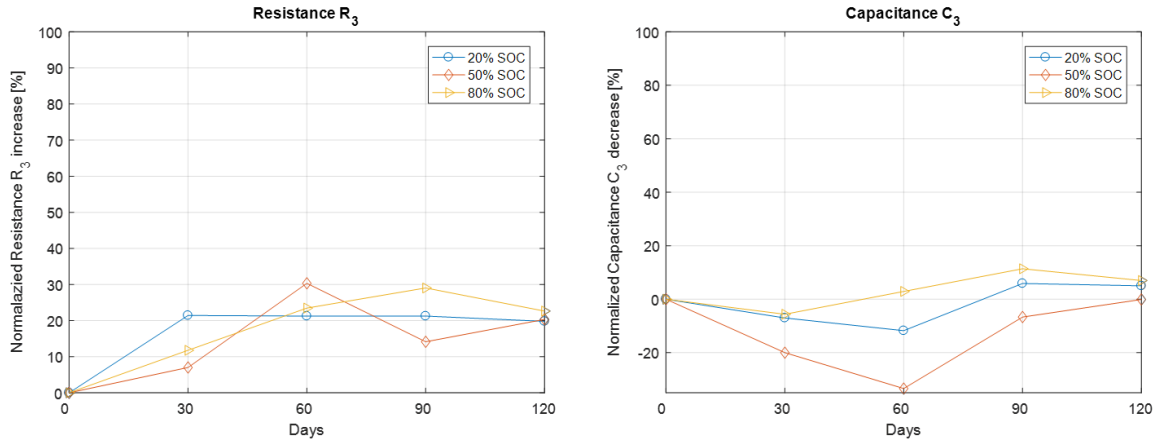


Figure 4.25: (left)Normalized increase of Resistance $R_3$ and decrease of $C_3$ based on BOL

### 4.3.2 Summary of EIS

Overall, as a conclusion with regards to the EIS measurement analysis, it was possible to diagnose the impedance increase and indicate the most sensitive parameters to ageing. These are the parameters $R_1$, $C_1$, and $R_2$, $C_2$ that followed a certain increasing trend along with calendar ageing. In other words the two semicircles of the EIS curves, that represent the SEI growth and the charge transfer resistance respectively. Parameters $R_1$, $C_1$ were measured between the high frequency (kHz) and mid frequency range (Hz) while parameters $R_2$, $C_2$ between the mid frequency (Hz) and low frequency range (mHz). However, the minimum and maximum frequency limits at each range are not constant with ageing, a fact that is possibly an outcome of the random inductive tail and shifting ohmic resistance. These parameters measured in the high frequency range determine the number of samples occupied in this region, and this phenomena which is exemplified in Figure 4.26 has a direct impact on the previous frequencies occupied by the parameters of interest.

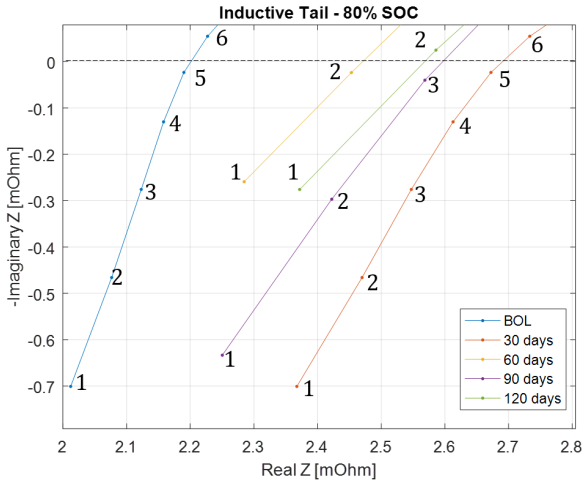


| | |
|---|---|
| 1 | $10kHz$ |
| 2 | $7.5858kHz$ |
| 3 | $5.7544kHz$ |
| 4 | $3.3113kHz$ |
| 5 | $2.5119kHz$ |
| 6 | $1.9055kHz$ |

Figure 4.26: Illustration of frequency points sampled at the inductive tail

# 5 | Simulation Results of PRBS

## 5.1 Impedance model

In this Chapter, the possibility of applying the PRBS signal to an impedance model is demonstrated through simulation. Engineering software such as PLECS and MATLAB were used for the creation of models and algorithms. The aim here is to validate this method by obtaining the data in a specific frequency range where the parameters of impedance follow the most certain trends can be obtained. In FIGURE 5.1 the impedance model that was used is illustrated.

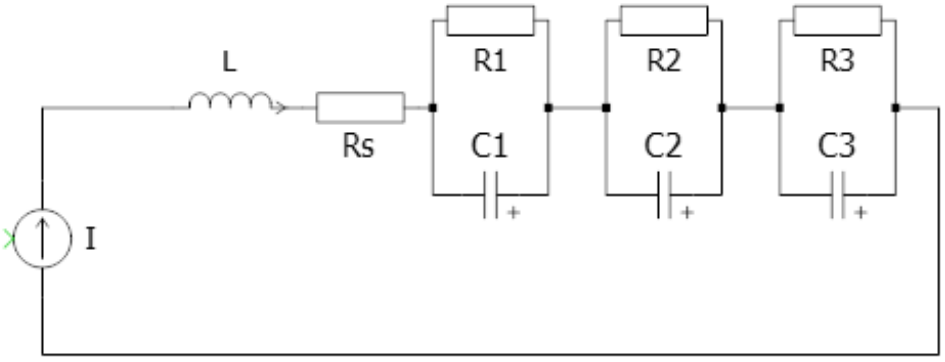


Figure 5.1: Impedance model

The initial values that the impedance model utilized for each component were taken from the EIS fitting model derived after 30 days of accelerated calendar. The EEC components and the corresponding values are presented in Table 5.1.

| **EEC Component** | **Value** |
|---|---|
| L | 1.1152e-08 |
| $R_s$ | 2.5683e-03 |
| $R_1$ | 0.9537e-03 |
| $C_1$ | 0.3 |
| $R_2$ | 1.140e-03 |
| $C_2$ | 10.035 |
| $R_3$ | 1.90557e-03 |
| $C_3$ | 0.9e+04 |

Table 5.1: The input values to the EEC components for the simulation test

## 5.2 Selection of PRBS parameters

From the previous analysis in section 4.3, the impedance parameters $R_1$, $C_1$ and $R_2$, $C_2$ are selected as the most dependant on the performed calendar ageing. Thus, as long as the EIS performed on the same cell is used as a reference, according to Table 4.4, the frequencies that would provide the data for each case are :

$$52.48Hz \; to \; 3.311kHz$$

and

$$363mHz \; to \; 120.22Hz$$

In both cases the clock frequency $f_c$ was determined by equation 3.12 and the number of bits for the design of PRBS were determined by equation 3.13. The final frequency range that was achieved to simulate, based on the useful frequency range determined by the 3-dB bandwidth is shown in table 5.2 for each case.

| **Case** | **Targeted impedance parameters** | **PRBS bits** | **Frequency range** | **Clock Frequency** |
|---|---|---|---|---|
| 1 | R1, C1 | 8-bits | 5.5 mHz : 5.5 mHz : 0.6321 Hz | 1.43 Hz |
| 2 | R2, C2 | 10-bits | 0.265 Hz : 0.265 Hz : 120.22 Hz | 272 Hz |

Table 5.2: Details for each case that the PRBS was designed for

In Figure 5.2(left) a period of the applied current controlled by the PRBS signal is illustrated, and in Figure 5.2 (right) the voltage response of the impedance model during this period is shown. However Figure 5.3 is also used to show a closer look due to the signals for easiness of comprehension. The useful frequency range based on the 3-dB rule is illustrated through the frequency response obtained from case 2 in Figure 5.4.

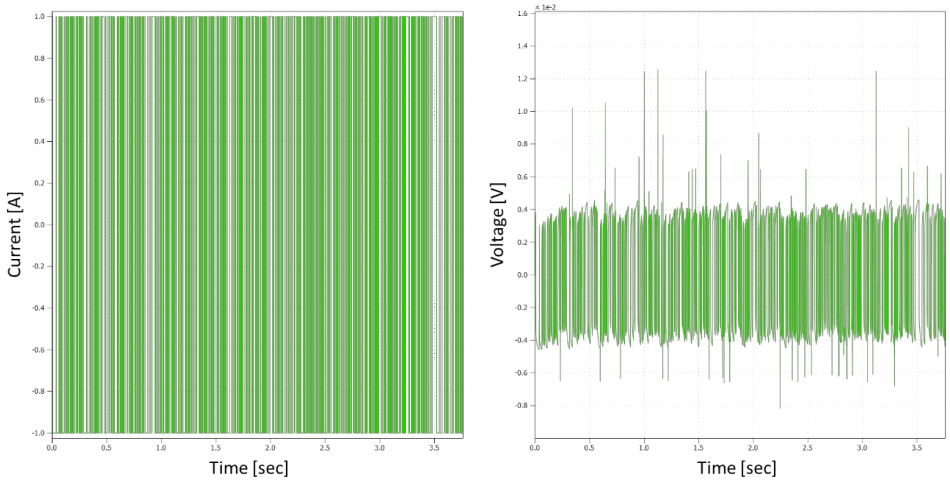


Figure 5.2: (Left) PRBS input current to case 2 (Right) Voltage response of impedance model of case 2

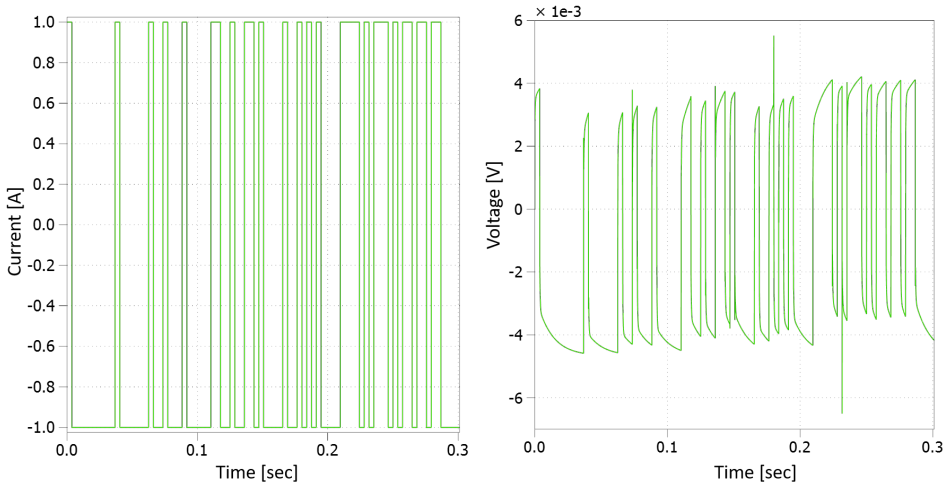


Figure 5.3: (Left) Zoom into PRBS input current to case 2 (Right)Zoom into Voltage response of impedance model of case 2

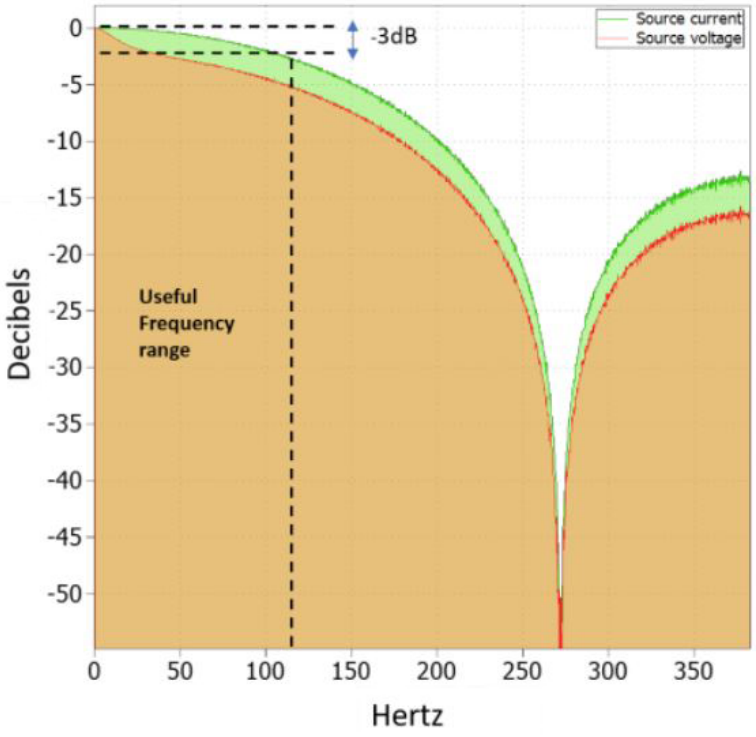


Figure 5.4: FFT of PRBS current input (green) and voltage response (red) of case 2

## 5.3 Impedance determination with PRBS

The PRBS is similar to a square wave as they are both composed of multiple superimposed sine waves. Thus, the impedance was determined by decomposing the input current signal and voltage response through the Fourier Transform according to [40]. The impedance was then

calculated by the ratio of the amplitude and phase coefficients at each corresponding frequency as shown in equation 5.1.

$$Z(\omega) = \frac{\widehat{U}(\omega)}{\widehat{I}(\omega)} \tag{5.1}$$

Where $\widehat{U}(\omega)$ and $\widehat{I}(\omega)$ are the Fourier transforms of the model's voltage response $U(t)$ and the current input $I(t)$. The code used in MATLAB for processing the sampled data after applying the PRBS signal is provided in the Appendix B. In Figure 5.5, the results by applying PRBS at case 1 and case 2 are shown along with the curve of the impedance model, while in Figure 5.6 the results of case 2 are presented also in Bode plot where the magnitude and phase are plotted along with the useful frequency range.

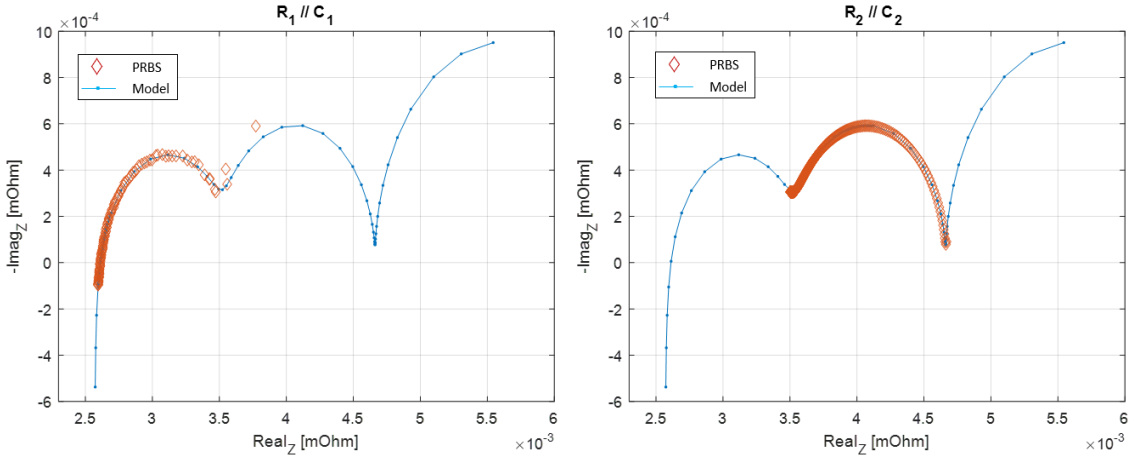


Figure 5.5: (left) Curve fitting of EIS model $R_1$ and $C_1$ by PRBS, (right) Curve fitting of EIS model $R_2$ and $C_2$ by PRBS

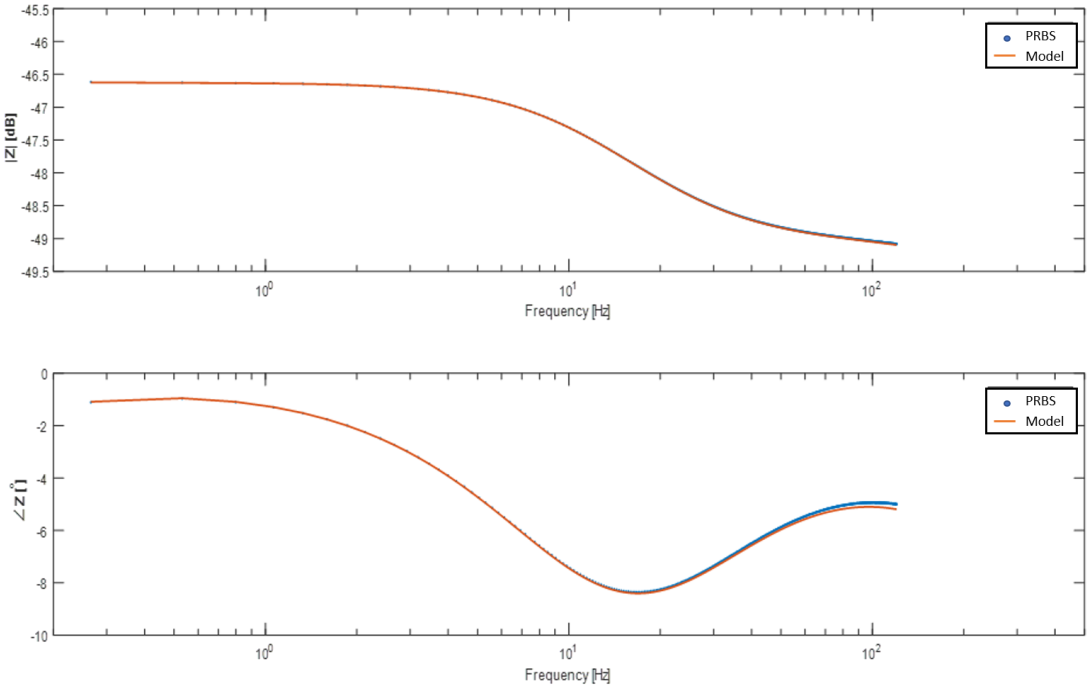


Figure 5.6: Bode plot of Model and PRBS simulation

Furthermore, in Figure 5.7 the possibility of monitoring the impedance increase of the specific parameters of interest along with calendar ageing is also shown. Moreover in Figure 5.8, the calendar ageing of the derived models in each age are compared along with the curve fitting performed by PRBS signals are presented.

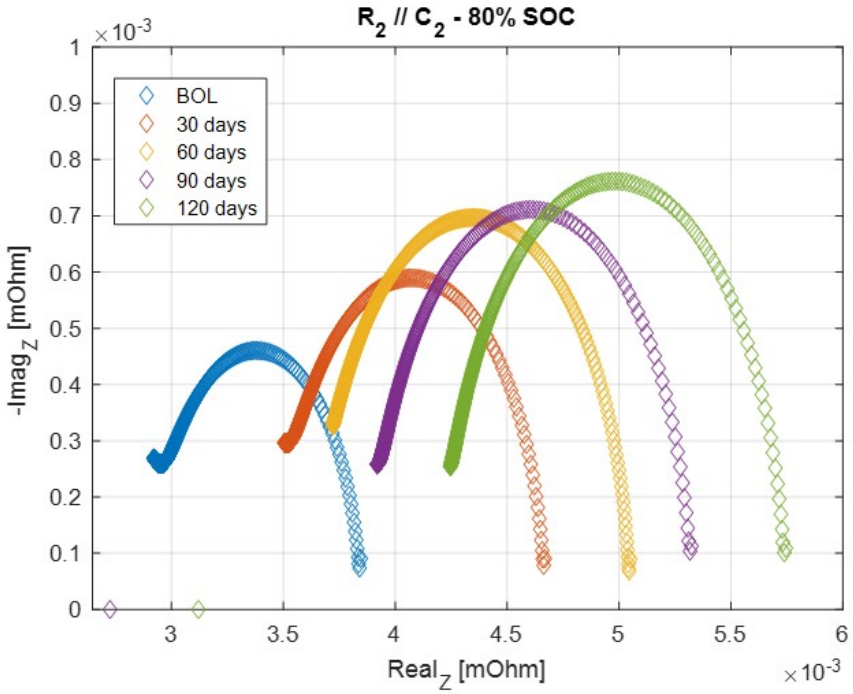


Figure 5.7: Calendar ageing of $R_2$ and $C_2$ at 80% SOC with PRBS

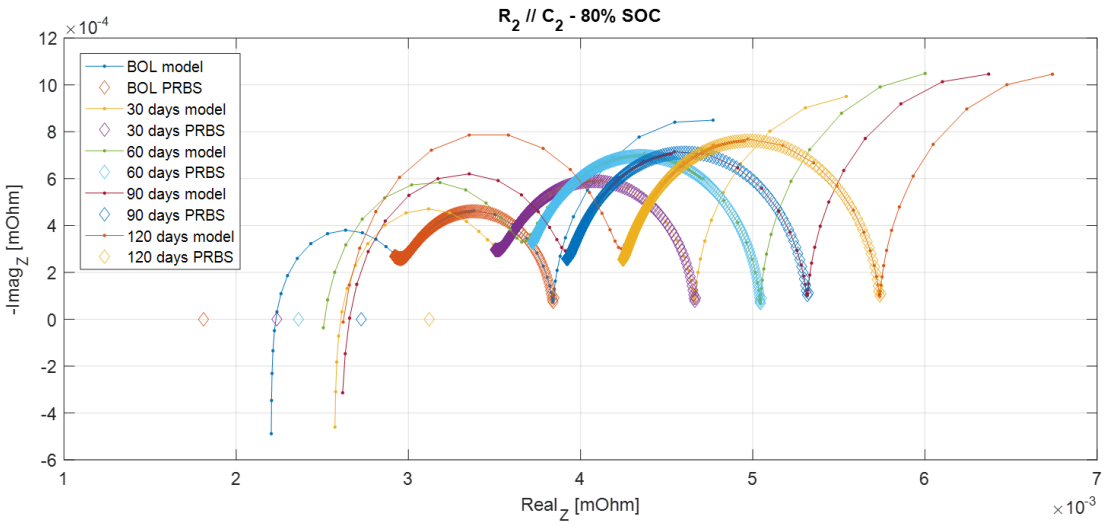


Figure 5.8: Calendar ageing of $R_2$ and $C_2$ at 80% SOC compared with the corresponding model of each age

### 5.3.1 Summary of PRBS simulation

As a conclusion with regards to the simulation process of PRBS, it has been demonstrated through the used software tools, that this method could be used as an alternative diagnostic tool, when the focus is on specific impedance parameters of a known frequency range. The impedance model based on which the PRBS was simulated, was curve fitted successfully and calendar ageing of impedance was also followed.

# 6 | Conclusion

This project focuses on evaluating results obtained from diagnostic methods of Lithium Ion Batteries. Two state-of-the-art methods were evaluated (a) DC currents pulses and (b) EIS that are theoretically described along with their measurement technique and furthermore applied on a tested cell as reference performance tests for the practical analysis. Another method (c), based on PRBS signals is tested in simulation software environment as an alternative candidate to perform impedance measurements that would provide equally useful data to EIS. Throughout the conducted analysis of each case the following findings were encountered.

- Through the DC current pulse technique, the dc internal resistance is obtained during an applied current pulse which increases with ageing and can be diagnosed by determining the resistance at the instantaneous current excitation moment, and at the transient voltage response. This analysis was carried out for both charge and discharge pulses. The dependency on ageing for each determined resistance has been monitored, and moreover the dependency that each investigated SOC level shows on ageing (20% , 50% and 80%) was presented.

- The $R_{ohmic}$ resistance gained most of the attention both as its contribution to the total internal resistance during an applied current pulse, but also as an increasing parameter with calendar ageing. At 50 % SOC, after 120 days of accelerated calendar ageing $R_{ohmic}$ showed more than 40% normalised increase based on BOL condition.

- Capacity checks measured with the Coulomb counting method did not show substantial capacity fade for the first 90 days of accelerated calendar ageing as it was 3.95%. However, after 120 days the capacity fade was calculated 7.38%. In terms of EV applications, where the maximum allowed capacity fade is 20%, these results are presented more meaningful as the SOH in these terms, reached 63.07% after 120 days.

- The degradation of Pulse Power Capability was measured for each charge and discharge pulse at each investigated calendar age, however this parameter was the most tolerant and the least affected by showing power fade of just 2-3% only during the 20s discharge pulse.

- Through the EIS method, the increase of ac impedance was diagnosed during the performed accelerated calendar ageing by decomposing to 8 impedance parameters.The impedance parameters were identified at different frequency ranges, and evaluated separately. The growth of SEI represented by $R_1$ and $C_1$ and the charge transfer resistance represented by $R_2$ and $C_2$ showed the most certain degradation with calendar ageing. The trends of these parameters influence the most the increase of ac impedance.

- Finally, in this project the PRBS method is validated in a simulation manner as an alternative technique to determine the ac impedance, when the frequency range of specific impedance parameters is known. The trends of these parameters where possible to monitor along with calendar ageing and where successfully compared with the impedance model curve derived from the EIS method.

.

# 7 | Future Works

The results of the PRBS in simulation environment show that impedance can be identified for a specific range of frequencies when the parameters of interest are known. The future work that can be conducted based on these results are the following:

- After the demonstrated simulation feasibility on a linear model, this method can be stepped up and be applied on a non-linear model which would resemble even more a future tested cell.
- In this work, the PRBS results where compared with the curve obtained by an impedance model from simulation point of view. If this work is finally applied on a real tested cell, further investigation on validated experimental results would be possible to compare with the actual curve of EIS measurements.
- Another aspect that would be interesting, would be to apply the PRBS technique during cycling ageing, while a current load is applied. This way, the measurement of impedance while various loads are charging or discharging, might be advantageous.

# 8 Appendix

## .1 Appendix A

The curve fitting by the derived impedance model is presented in the following figures for all encounter calendar ages.

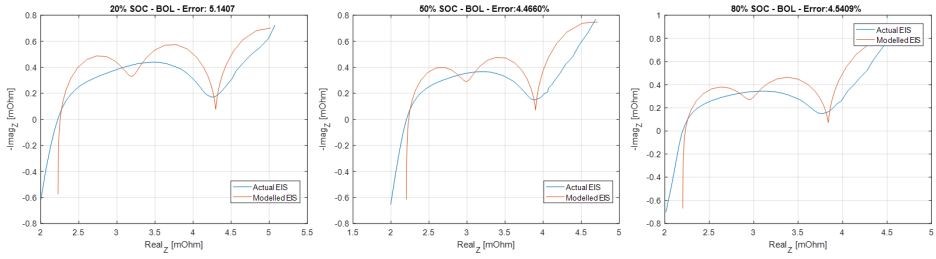


Figure .1: Illustration of the impedance model curve compared with the actual impedance curve for BOL (Left) 20% SOC, (Middle) 50% SOC (Right) 80% SOC


Figure .2: Illustration of the impedance model curve compared with the actual impedance curve after 1 month of calendar ageing (Left) 20% SOC, (Middle) 50% SOC (Right) 80% SOC


Figure .3: Illustration of the impedance model curve compared with the actual impedance curve after 2 months of calendar ageing (Left) 20% SOC, (Middle) 50% SOC (Right) 80% SOC


Figure .4: Illustration of the impedance model curve compared with the actual impedance curve after 3 months of calendar ageing (Left) 20% SOC, (Middle) 50% SOC (Right) 80% SOC


Figure .5: Illustration of the impedance model curve compared with the actual impedance curve after 4 months of calendar ageing(Left) 20% SOC, (Middle) 50% SOC (Right) 80% SOC

## .2 Appendix B

The code with the algorithm that was used in MATLAB in order to perform the FFT analysis of the input current, and voltage response of the impedance model, after the application of PRBS signal, is shown below.

```
%% PRBS characteristics
n = 10 ;                % Number of bits for the PRBS
N = 2^n - 1 ;           % PRBS signal length
fc = 2.72e2;            % Clock pulse frequency of the PRBS
f_delta = fc/N ;        % Distance between power frequencies in the spectrum
f_min = f_delta ;       % Minimum frequency in the PRBS signal
f_max = 0.442*fc ;      % -3 dB limit frequency for the band-width limited white noise
                            approximation of the PRBS
T_min = 1/f_min ;       % Minimum time necessary for the FFT to detect f_min

Nc = 1 ;                % Number of cycles to be used for the FFT calculations

%% Define data structures and perform the FFT
FFT_V = FFTDATA(t,V) ;
FFT_V.cycles = Nc ;
FFT_V.fundamental = f_min ;
FFT_V.maxFrequency = f_max ;

FFT_V = power_fftscope(FFT_V) ;
FFT_V.freq = FFT_V.freq(1:Nc:end) ;
FFT_V.mag = FFT_V.mag(1:Nc:end) ;
FFT_V.phase = FFT_V.phase(1:Nc:end) ;

FFT_I = FFTDATA(t,I) ;
FFT_I.cycles = Nc ;
FFT_I.fundamental = f_min ;
FFT_I.maxFrequency = f_max ;

FFT_I = power_fftscope(FFT_I) ;
FFT_I.freq = FFT_I.freq(1:Nc:end) ;
FFT_I.mag = FFT_I.mag(1:Nc:end) ;
```

```
FFT_I.phase = FFT_I.phase(1:Nc:end) ;

%% Calculate impedance from voltage and current fourier coeficients
Z = FFT_V.mag./FFT_I.mag .* (cosd(FFT_V.phase - FFT_I.phase) + 1i*sind(FFT_V.phase -
    FFT_I.phase)) ;

%% Impedance based model of the battery
s = tf('s') ;

Rs = 2.201e-03 ;
L = 1.1152e-08 ;
Z_L = Rs + s*L ;

R1 = 0.7580e-03 ;
C1 = 0.5013 ;
Z_C1 = R1/(s*C1*R1 + 1) ;

R2 = 0.880140e-03 ;
C2 = 14.2543;
Z_C2 = R2/(s*C2*R2 + 1) ;

R3 = 1.70490e-03;
C3 = 0.852052e+04 ;
Z_C3 = R3/(s*C3*R3 + 1) ;

Zeq = Z_L + Z_C1 + Z_C2 + Z_C3 ;

Zeq_w = freqresp(Zeq,FFT_V.freq,'Hz') ;
Zeq_w = Zeq_w(:) ;

%% Compare the results in bode plot
figure('Name','Bode plot to compare simulation results and impedance model','NumberTitle'
    ,'off','units','normalized','outerposition',[0 0 1 1])
warning('off','MATLAB:HandleGraphics:ObsoletedProperty:JavaFrame');
pause(10e-6);
frame = get(handle(gcf),'JavaFrame');
set(frame,'Maximized',1);

subplot(2,1,1)                              % Magnitude plot of the data and model
semilogx(FFT_V.freq,mag2db(FFT_V.mag./FFT_I.mag),'.','MarkerSize',6)
hold on
semilogx(FFT_V.freq,mag2db(abs(Zeq_w)),'LineWidth',1.5)
xlabel('Frequency [Hz]')
ylabel('\bf |Z| [dB]')
legend('Simulation','Model')
xlim([0.2 500])

subplot(2,1,2)                              % Phase plot of the data and model
semilogx(FFT_V.freq,unwrap((FFT_V.phase-FFT_I.phase)*pi/180)*180/pi,'.','MarkerSize',6)
hold on
semilogx(FFT_V.freq,real(-1i*log(Zeq_w./abs(Zeq_w)))*180/pi,'LineWidth',1.5)
xlabel('Frequency [Hz]')
ylabel('\bf \angle Z [^\circ]')
legend('Simulation','Model')
xlim([0.2 500])
```

# Bibliography


[1] Markkus Rovito. The 2016 volvo xc90 t8 twin engine phev enters the us market with great promise. *CHARGED Electric vehicle magazine*, 2015. URL=https://chargedevs.com/features/the-2016-volvo-xc90-t8-twin-engine-phev-enters-the-us-market-with-great-promise/.

[2] MpowerUK. Battery performance characteristics. URL `http://www.mpoweruk.com/performance.htm`.

[3] J.-M. Tarascon and M. Armand. "issues and challenges facing rechargeable lithium batteries,". *Nature*, vol. 414, 2001.

[4] Daniel-Ioan Stroe Remus Teodorescu Søren Juhl Andreasen Ana-Irina Stan, Maciej Swierczynski. "lithium ion battery chemistries from renewable energy storage to automotive and back-up power applications - an overview". Technical report, Department of Energy Technology, Aalborg University, Denmark, 2014.

[5] A. Stan D. Stroe and R. Teodorescu. "accelerated lifetime testing methodology for lifetime estimation of lithium-ion batteries used in augmented wind power plants,". *IEEE TRANSACTIONS ON INDUSTRY APPLICATIONS*, 50(6), nov 2014.

[6] Y.P. Chen-Y.C. Hsieh K.S. Ng, C.S. Moo. Enhanced coulomb counting method for estimating state-of-charge and state-of-health of lithium-ion batteries. *Applied Energy*, 86, 2009.

[7] Richtek. "understanding the characteristics of li-ion batteries and richtek power management solutions,", 2014. URL `http://www.richtek.com/en/Design%20Support/Technical%20Document/AN023,`.

[8] Wei He Nicholas Williard Chaochao Chen Michael Pecht. State of charge estimation for electric vehicle batteries using unscented kalman filtering. *Microelectronics Reliability*, 53 (6):840–847, 2013.

[9] K. Makinejad S. Thanagasundram, R. Arunachala and T. Teutsch. A cell level model for battery simulation, 2012.

[10] Jianqiu Li Guangming Liu, Languang Lu and Minggao Ouyang. Thermal modeling of aifepo 4/graphite battery and research on the influence of battery temperature rise on ev driving range estimation. *IEEE*, page 1–5, 2013.

[11] J. Macdonald S. Saxena, C. Le and S. Moura. Quantifying ev battery end-of-life through analysis of travel needs with vehicle powertrain models. *Journal of Powe Sources*, 282 (265-276), 2015.

[12] Jae Moon Lee Bo Hyung Cho Jong Hoon Kim, Seong Jun Lee. A new direct current internal resistance and state of charge relationship for the li-ion battery pulse power estimation. Technical report, Seoul National University Department of Electrical Engineering, 2007.

[13] L.D. Whitcanack R.C. Ewell B.V. Ratnakumar, M.C. Smart. The impedance characteristics of mars exploration rover li-ion batteries. *Journal of Power Sources*, 159: 1428–1439, 2006.

[14] S. Juhl D. I. Stroe M. Swierczynski A. I. Stan V. Knap R. Teodorescu D. Loan, M. Jozef and S. J. Andreasen. "diagnosis of lithium-ion batteries state-of-health based on electrochemical impedance spectroscopy technique,". Technical report, Department of Energy Technology, Aalborg University, 2014.

[15] M. Swierczynskia T. Stanciua R. Teodorescua A.-I.Stroea, D-I. Stroea and S. K. Kæra. The ac impedance characteristic of high power li4ti5o12-based battery cells. *ECS Transactions*, 70(1):840–847, 2015.

[16] Charalampos Savvidis Zeyang Geng. Onboard impedance diagnostics method of liion traction batteries using pseudo-random binary sequence. Master's thesis, Linköping University, 2015.

[17] United Nations. Adoption of the paris agreement, December 2015.

[18] Stephen Castle. Britain to ban new diesel and gas cars by 2040. *The New York Times*, 2017. URL `https://www.nytimes.com/2017/07/26/world/europe/uk-diesel-petrol-emissions.html`.

[19] Volvo Car Group. Volvo cars to go all electric, jul 2017. URL `https://www.media.volvocars.com/global/en-gb/media/pressreleases/210058/volvo-cars-to-go-all-electric`.

[20] T. Trigg M. Lowe, S. Tokuoka and G. Gereffi. "lithium-ion batteries for electric vehicles,". Technical report, Center of Globalization, Governance & Competitiveness, Duke University, 2010.

[21] Thomas B. Reddy David Linden. *Handbook of batteries*, volume 3rd Edition. McGraw-Hil, 2001.

[22] Sigit Agung Widayat Lora Khaula Amifia Adha Cahyadi * Oyas Wahyunggoro M. Nisvo Ramadan, Bhisma Adji Pramana. Comparative study between internal ohmic resistance and capacity for battery state of health estimation. *Journal of Mechatronics, Electrical Power, and Vehicular Technology*, 06:113–122, 2015.

[23] Rahul Gopalakrishnan Jean-Marc Timmermans Noshin Omar Peter van den Bossche Alexandros Nikolian *, Yousef Firouz and Joeri van Mierlo. Lithium ion batteries—development of advanced electrical equivalent circuit models for nickel manganese cobalt lithium-ion. *Energies*, may 2016.

[24] A. Zenati et al. A methodology to assess the state of health of lithium-ion batteries based on the battery ' s parameters and a fuzzy logic system. *IECON 2010*, 2010.

[25] Jianqiu Li a Jianfeng Hua b Minggao Ouyang a Languang Lu a, Xuebing Han a. A review on the key issues for lithium-ion battery management in electric vehicles. *Journal of Power Sources*, 226, nov 2013.

[26] C. Fleischer W. Waag and D. Uwe. "critical review of the methods for monitoring of lithium-ion batteries in electric and hybrid vehicles,". *Journal Power Sources*, 258:321–339, 2014.

[27] K. Lee K. L. Duncan and E. D. Wachsman. "dependence of open-circuit potential and power density on electrolyte thickness in solid oxide fuel cells with mixed conducting electrolytes,". *Journal Power Sources*, 196(5):2445–2451, 2011.

[28] G. V Avvari B. Pattipati, B. Balasingam and K. R. Pattipati. "open circuit voltage characterization of lithium-ion batteries,". *Journal Power Sources*, 269:317–333, 2014.

[29] Daniel Stroe. Battery testing for performance modelling. Conversion and Storage in Future Energy Systems at Aalborg University, Energy Department, 2017.

[30] Julia Drillkens a c Philipp Sinhuber a c Dirk Uwe Sauer a b c Andrea Marongiu a, c. A critical overview of definitions and determination techniques of the internal resistance using lithium-ion, lead-acid, nickel metal-hydride batteries and electrochemical double-layer capacitors as examples. *Joutnal of Power Sources*, jul 2015.

[31] D.-I. Stroea R. Teodorescua S.K. Kær A.-I. Stroea, M. Swierczynskia. Pulse power capability estimation of lithium titanate oxide-based batteries. *ECS Transactions*, 74: 45–53, 2016.

[32] O. Komesker-A. Raschke M. Schiemann C. Zehner M. Gehnen M. Keller H. Schweiger, O. Obeidi and P. Birke. Comparison of several methods for determining the internal resistance of lithium ion cells. *Sensors*, page 5604–5625, 2010.

[33] IEEE Min Chen, Student Member and IEEE Gabriel A. Rincon-Mora, ´ Senior Member. Accurate electrical battery model capable of predicting runtime and i–v performance. *IEEE TRANSACTIONS ON ENERGY CONVERSION*, 21(2):504–511, 2006.

[34] Daniel Stroe. Performance modeling of batteries. Lecture 9,for course Conversion and Storage in Future Energy Systems at Aalborg University, Energy Department, 2017.

[35] M. Meiler a K. Steiner a Ch. Wimmer a T. Soczka-Guth a D.U. Sauer D. Andre a, . Characterization of high-power lithium-ion batteries by electrochemical impedance spectroscopy. i. experimental investigation. *Journal of Power Sources*, 196:5334–5341, 2011.

[36] MATTIA RICCO. *FPGA-Based Implementation of Real-Time Identification Procedures for Adaptive Control in Photovoltaic Applications*. PhD thesis, Université de Cergy-Pontoise, 2015.

[37] M. P. Foster A. J. Fairweather and D. A. Stone. Battery parameter identification with pseudo random binary sequence excitation ( prbs ). *Journal Power Sources*, 196(22): 9398–9406, 2011.

[38] Biljana Mileva Boshkoska Pavle Boškoski, Andrej Debenjak. *Fast Electrochemical Impedance*. Springer, 2017.

[39] Nataliya Lvovna Shcherbakova Anton Pavlovich Tyukov Timur Alexandrovich Janovsky Maxim Vladimirovich Shcherbakov, Adriaan Brebels and Valeriy Anatol'evich Kamaev. A survey of forecast error measures. *World Applied Sciences Journal*, 24, 2013.

[40] Xiao-Zi Yuan · Chaojie Song · Haijiang Wang Jiujun Zhang. *Electrochemical Impedance Spectroscopy in PEM Fuel Cells Fundamentals and Applications*. Springer, 2010.